



# Geochemistry of indium in magmatic-hydrothermal tin and sulfide deposits of the Herberton Mineral Field, Australia

Avish A. Kumar<sup>1</sup> · Ioan V. Sanislav<sup>1</sup> · Henrietta E. Cathey<sup>2</sup> · Paul H. G. M. Dirks<sup>1</sup>

Received: 14 September 2022 / Accepted: 2 May 2023 / Published online: 23 May 2023  
© The Author(s) 2023

## Abstract

The Herberton Mineral Field in Northeast Australia hosts world class magmatic-hydrothermal Sn–W polymetallic deposits that are enriched in In. The Baal Gammon and Isabel deposits from the Herberton Mineral Field contains early tin, as cassiterite, overprinted by sulfide mineralization as chalcopyrite, sphalerite, galena, pyrrhotite, and stannite. We investigated the distribution of In in the sulfide ores from these two deposits, calculated the temperature of formation via sphalerite-stannite geothermometer, and deduced the physicochemical conditions favorable for enriching In in this mineralizing environment. The Baal Gammon deposit is dominated by chalcopyrite, with In contained in chalcopyrite, sphalerite, and stannite. The average In concentrations measured by EPMA in chalcopyrite, sphalerite, and stannite are 0.10, 0.68, and 0.92 wt%, respectively. Chalcopyrite, pyrrhotite, and sphalerite textures indicate that In incorporation occurred during exsolution from an intermediate solid solution of cubanite composition. The Isabel deposit is dominated by sphalerite associated with galena and contains only minor amounts of chalcopyrite. The average concentration of In in sphalerite from the Isabel deposit is 0.11 wt%. The stannite-sphalerite geothermometer indicates mineralization temperatures of ~290 °C at the Baal Gammon deposit, and ~307 °C at the Isabel deposit. At these temperatures, the physicochemical modeling suggests that stable In chlorine complexes occur in acidic conditions (pH < 3). These results when combined with the Eh–pH phase model of the sulfide assemblage further constrain the redox conditions during mineralization.

**Keywords** Indium · Tin · Critical metals · Physicochemical modeling · Queensland

## Introduction

Indium (In) is used in the production of flat panel displays, touchscreens, photovoltaic cells, and fiber optic technology, and is considered a critical metal (Frenzel et al. 2017; Watari et al. 2020; Fontana et al. 2021). Indium occurs in a variety of deposit styles that includes epithermal, tin (Sn) polymetallic, skarn, porphyry, volcanogenic massive sulfide, sedimentary exhalative, and granite-related

deposits (Schwarz-Schampera and Herzig 2002; Seifert and Sandmann 2006; Ishihara et al. 2011; Werner et al. 2017; Carvalho et al. 2018). These deposits are magmatic-hydrothermal in origin and although a link between In and hydrothermal fluids is inferred, the geochemical conditions that concentrate In in magmatic-hydrothermal systems are not well understood. In these deposits, In is mainly incorporated in base-metal sulfides such as sphalerite, and chalcopyrite, and rarely forms roquesite which is the primary In mineral (Andersen et al. 2016; Bauer et al. 2019b). The distribution of In in sulfide ores has been well studied and multiple authors have come to the conclusion that sphalerite and occasionally chalcopyrite incorporate In by coupled substitution reactions in hydrothermal conditions (Sinclair et al. 2006; Cook et al. 2012; Murakami and Ishihara 2013; Valkama et al. 2016; George et al. 2018; Bauer et al. 2019a; Torró et al. 2019b; Xu et al. 2021). In polymetallic Sn deposits, high concentration of In is found in stannite, which is an alteration product of cassiterite (Murakami and Ishihara 2013; Andersen et al. 2016; Torres

Editorial handling: F. Melcher

✉ Avish A. Kumar  
avish.kumar@my.jcu.edu.au

<sup>1</sup> Economic Geology Research Centre (EGRU), College of Science and Engineering, James Cook University, Townsville, Australia

<sup>2</sup> Central Analytical Research Facility (CARF), School of Earth and Atmospheric Sciences, Queensland University of Technology, Brisbane, Australia

et al. 2019). Stannite-sphalerite mineral pairs can be used as a geothermometer, and the results are comparable to fluid inclusion studies (Sinclair et al. 2006; Nekrasov et al. 1979; Shimizu and Shikazono 1985). Thus, the paragenesis of sulfide ores and the distribution of In in different sulfide minerals can be used to infer the physicochemical conditions during mineralization.

The Baal Gammon and Isabel deposits are located in the Herberton Mineral Field, Queensland, Australia (Fig. 1), and are known for In reserve in the region (Kumar et al. 2022). Both deposits contain a similar mineral assemblage consisting of cassiterite overprinted by polymetallic sulfides. In this study, we use mineral paragenesis combined with high-resolution compositional mapping and mineral chemistry to understand the distribution of In between different ore minerals. These results are then integrated with geochemical modeling to infer the physicochemical conditions that lead to In enrichment in these deposits.

## Geological background

The HMF is situated centrally in the Mossman Orogen (Fig. 1; Henderson et al. 2013; Henderson and Fergusson 2019). The dominant geological units at the HMF are the metasedimentary rocks of the Hokinson Formation intruded by the Carboniferous to Permian plutonic and volcanic rocks of the Kennedy Igneous Association (Poblete et al. 2017; Edgar et al. 2022a, b). The Hodgkinson Formation consists of deformed turbidite that were deposited in a deep-marine environment and metamorphosed to greenschist and amphibolite facies (Henderson et al. 2013). The granitoids have been grouped into three supersuites and include, from oldest to youngest, the O'Briens Creek, Ootan, and Almaden supersuites (Champion 1991; White et al. 2001; Cheng et al. 2018). The Koolmoon Volcanic Group consists of the Slaughter Yard Creek, and the Featherbed volcanics, but only the former occurs in the vicinity of the Baal Gammon and Isabel deposits. The Slaughter Yard Creek Volcanics consist of a series of rhyolite dykes, rhyolitic flows, and volcanoclastic rocks (Fig. 1; Kumar et al. 2022).

### The geology of the Baal Gammon and Isabel deposits

The Baal Gammon deposit occurs along the contact between the Hodgkinson Formation and a quartz-porphyry dyke (the UNA Porphyry). The Hodgkinson Formation at the Baal Gammon deposit consists of greenschist facies sandstones that were gently folded and are crosscut by a series of low-angle thrusts and steeply dipping transcurrent faults. Near the UNA Porphyry contact, the meta-sandstones contain garnet and andalusite indicating contact metamorphism.

The meta-sandstone at the deposit dips  $\sim 10^\circ$  towards SW. The UNA Porphyry consists of quartz phenocrysts in a finer grained mass of felspar, quartz, and minor biotite. The biotite is usually chloritized, and the feldspar is sericite altered. The UNA porphyry has an irregular shape and dips  $\sim 40^\circ$  towards south. The entire sequence is crosscut by felsic porphyry dykes of the Slaughter Yard Creek Volcanics (Fig. 1b).

The Isabel deposit is hosted by brecciated quartzite of the Hodgkinson Formation. The quartzite unit is part of a metasedimentary sequence dominated by meta-sandstone with rhythmic intercalations of meta-siltstones. The metasedimentary sequence dips  $75^\circ$  east and is crosscut by multiple faults and lineaments (Kumar et al. 2022). The quartzite is iron stained, and chlorite and sericite altered. Both fault and hydrothermal breccias are common at the deposit. Very few ore minerals were observed in the fault breccia, whereas the hydrothermal breccia contains significant amount of sulfides. A few meters south from the deposit occurs the Herberton Hill Granite (Fig. 1c). The contact between the Herberton Hill Granite and the Hodgkinson Formation appears to be along a fault that trends NE. The granite is coarse grained, rich in feldspar and weathered, with feldspar tuned to clays and iron oxide films formed around quartz grain boundaries. The metasedimentary sequence and the granite are intruded by porphyry dykes assigned to the Slaughter Yard Creek Volcanics.

## Methods

### Petrography and sampling methods

Representative ore samples from drill core were selected and prepared (22 polished thin sections and five polished resin blocks) for the study of mineral textures and composition by reflected light microscopy, imaging by scanning electron microscope (SEM), and microanalysis by field emission electron probe microanalyzer (FE-EPMA). A Zeiss Primotech microscope was used to study the ore mineralogy under reflected light, and a Hitachi SU5000 SEM was used for further characterization of the minerals at the Advanced Analytical Centre of the James Cook University. Mineral textures were documented with backscattered electron (BSE) imaging, and energy-dispersive spectroscopy was used for preliminary elemental maps and spot analyses. The SEM detects In and other heavy metals (atomic weight  $> 20$  amu.) at concentrations greater than 0.5 wt%, allowing for identification and location of In-rich minerals prior to quantification with the FE-EPMA.

### Analytical methods

Quantitative compositional analyses were acquired using a JEOL JXA 8530F field emission microprobe at the Central

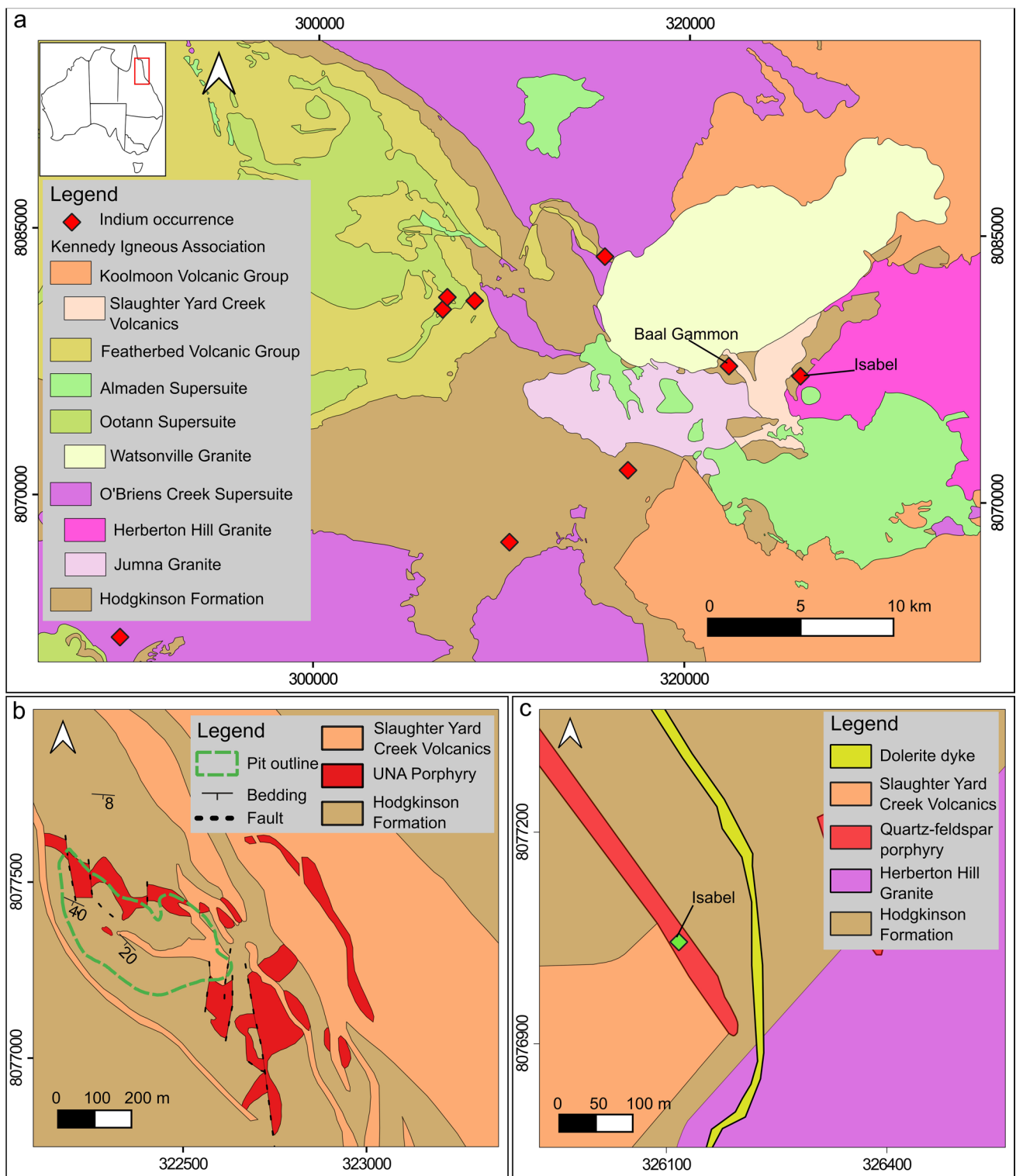


**Fig. 1** Simplified geological maps of **a** the Herberton Mineral Field; **b** the Baal Gammon deposit; and **c** the Isabel deposit

Analytical Research Facility at the Queensland University of Technology, Queensland, Australia. The instrument is equipped with five wavelength-dispersive (WD) spectrometers and Probe for EPMA software (Eugene, OR, USA) for data

acquisition and analysis. For in situ spot analysis, operating conditions were 20-kV accelerating voltage, 35-nA beam current, and a 1- $\mu$ m-diameter defocused beam (see Bauer et al. 2019b). Sample minerals include oxides (cassiterite)

and sulfides (sphalerite, chalcopyrite, pyrrhotite, stannite, galena, and arsenopyrite) that were analyzed using a selection of in-house and Astimex standards as calibration materials. Supplementary information 1 details the configuration of analyzing crystals on the five spectrometers and X-ray lines used for 14 elements of interest (S, Fe, Co, Cu, Zn, Ga, As, Se, Ag, Cd, In, Sn, Sb, and Pb), as well as calibration standards, peak and background counting times, detection limits (3 s), and elements included in the analytical routine for each phase. For all standards and sample minerals, detailed wavescans were acquired for each element in the analytical routine, encompassing wide background positions either side of the analytical peaks in order to assess peak interferences, optimize background positions, and model background curvature. The off-peak correction method was linear for all elements but Cu, As, Se, Al, and Sb, for which an exponential fit was preferred. Oxygen was calculated by stoichiometry for cassiterite and included in the matrix correction. Spectral interferences were fully quantified and element concentrations corrected using the Probe for EPMA software, which employs interference standards along with primary standards as part of the calibration process. The software performs quantitative correction for the matrix effects of the interference standards relative to the unknowns in the iterative data reduction algorithm, for improved accuracy compared to post-matrix corrections via subtraction (Donovan et al. 1993; Llovet et al. 2021). Interference corrections were applied for In  $L\alpha$  by Sn  $L\alpha$ , Cd  $L\alpha$  by In  $L\alpha$ , and Co  $K\alpha$  by Fe  $K\beta$ , by measuring background-corrected X-ray intensities on the interference standards at the spectrometer positions for the relevant interfered element emission lines. In this case, Sn metal, In metal, and troilite served as primary standards for measurement of Sn  $L\alpha$ , In  $L\alpha$ , and Fe  $K\alpha$  intensities, and also served as interference standards for intensity measurements at the positions of the In  $L\alpha$ , Cd  $L\alpha$ , and Co  $K\alpha$  lines respectively. Matrix-corrected interferences in secondary standards (Supplementary information 2) convert to  $\sim 10$  ppm In per 1 wt% Sn, and 9–10 ppm Co per 1 wt% Fe. Uncorrected data for cadmium are within analytical error of the corrected values. The detection limit (for In in most minerals is  $\leq 140$  ppm, and for other trace elements generally 100–300 ppm; Supplementary information 1). The  $\Phi(\rho z)$  matrix correction method of Pouchou and Pichoir-Full (Pouchou and Pichoir 1991) was used with the LINEMU database of mass absorption coefficients (Henke et al. 1993) for quantification. Data reproducibility and quality control were monitored by secondary standards (chalcopyrite, sphalerite, arsenopyrite, galena, cassiterite) that bracketed the unknowns in the analytical session (Supplementary information 2).

Semi-quantitative, background-corrected, WDS stage maps of In distribution in  $300 \times 300 \mu\text{m}^2$  areas in selected grains of chalcopyrite, sphalerite, pyrrhotite, and stannite

were collected at an accelerating voltage of 15 kV, a beam current of 60 nA, and at a 1- $\mu\text{m}$  step size (defocused beam diameter) with 200-ms dwell time per pixel, using the JEOL Map Analysis software. Five elements per map area were collected simultaneously in a single pass, followed by a second pass for background intensities, with the choice of elements in addition to In depending on the mineral phase (Sn, Cu, Zn, Fe, and In in sphalerite; Sn, Cu, Fe, Cd, and In in pyrrhotite and chalcopyrite; and Sn, Cu, Zn, Ag, and In in stannite). Additional high-resolution maps (beam scan mode) showing the distribution of Cu, Zn, Sn, Cd, and In were collected for a  $45 \times 45 \mu\text{m}^2$  area encompassing a representative grain boundary between chalcopyrite, pyrrhotite, and sphalerite in a massive sulfide sample from Baal Gammon to image In-rich exsolution lamellae and/or inclusions at the sub-micron scale. Conditions were 6-kV accelerating voltage, 60-nA beam current, fully focused beam, and 300-ms dwell time ( $\approx 170$  nm per pixel). The interaction volumes for chalcopyrite, pyrrhotite, and sphalerite under these conditions are  $\sim 300$  nm, with spatial resolution for the  $L\alpha$  X-ray signals of In, Sn, and Cd less than 170 nm based on Monte Carlo simulations using the CASINO software (Drouin et al. 2007).

## Geochemical modeling methods

Geochemical modeling of  $\text{InCl}^{++}$  complex and sulfide mineral formation was conducted with The Geochemist's Workbench (GWB) Community Edition 13 (Bethke et al. 2022) software. This allowed us to investigate the redox and pH conditions associated to In-rich sulfides and the stability of  $\text{InCl}^{++}$  complex over a range of temperature common in hydrothermal systems. The thermodynamic parameters ( $\Delta G_f$  and  $K_{eq}$ ) for modeling were obtained from the default geochemical database in the GWB software in combination with the Thermoddem (Blanc et al. 2012; Boschetti 2023). Copper, Zn, Fe, and In metal species were modeled at concentrations ( $10^{-6}$  M) similar to those observed in active hydrothermal systems (e.g., Seward et al. 2014; Simmons et al. 2016). We assumed the concentration of In to be  $< 10^{-6}$  M in hydrothermal waters since no analytical measurements exist according to our knowledge.

## Results

### Petrography and mineral paragenesis

Based on crosscutting and overprinting relationships, two primary mineralization stages (stages I and II; Figs. 2 and 3a) and a late supergene stage (stage III) were recognized at the Baal Gammon deposit. Stage I consists of cassiterite in the UNA Porphyry, and stage II consists of massive to semi-massive

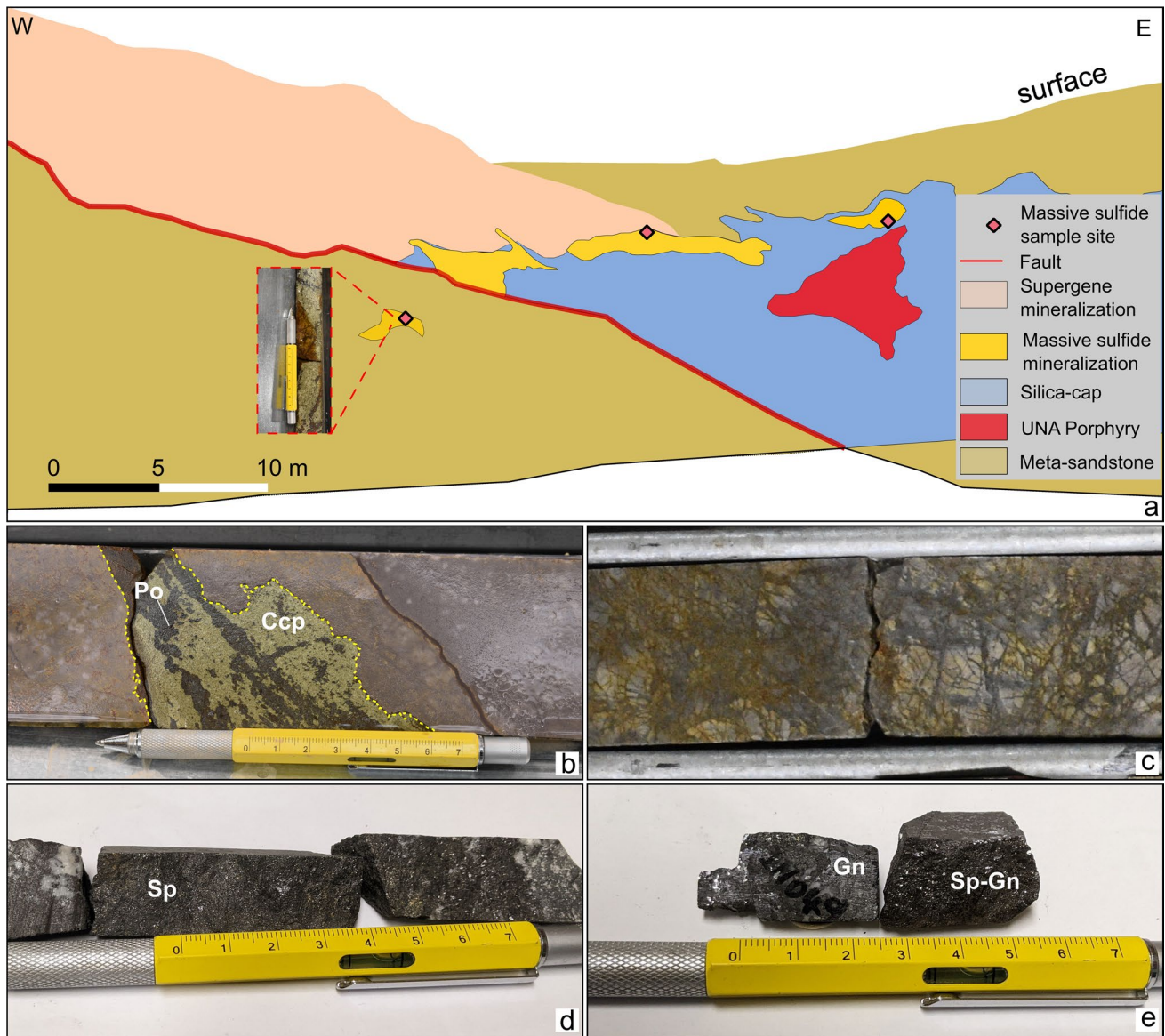


**Fig. 2** **a** Geological sketch map of the northern pit wall of the Baal Gammon deposit. **b** Diamond drill core image of the UNA Porphyry crosscut by sulfide vein. **c** Hydrothermal breccia of meta-sandstone

clasts in the Baal Gammon deposit. **d** Type 1 sphalerite veins from the Isabel deposit. **e** Type II veins consisting of galena and sphalerite from the Isabel deposit

sulfides, breccia infill, and disseminated sulfides (Fig. 2b, c). Stage III occurs in supergene zones and is composed of Cu oxides and carbonates, and Fe oxides. The supergene zones are not well developed or have been mined out, and only the interface between the leached zone (Fe oxides) and oxidized zones (Cu oxides and carbonates) were observed.

Stage I consists of cassiterite in veins and disseminated within the UNA Porphyry and locally within the meta-sandstone. The cassiterite grains typically occur together with chlorite, quartz, plagioclase, and magnetite (Fig. 4a). The cassiterite grains are several hundred microns across and consist of euhedral to subhedral crystals. They display concentric zoning consisting of alternating light and dark

brown bands under plane polarized light. Within the massive sulfide zones, the cassiterite grains commonly occur in clusters and consist of subhedral to anhedral crystals with corroded margins (Fig. 4b). Locally in the massive sulfide zones, the cassiterite grains are partially altered to stannite (Fig. 4b). In the proximity of the sulfide mineralization, some cassiterite and magnetite grains contain fractures infilled with chalcopyrite and/or pyrrhotite.

Stage II consists of sulfides that overprint the cassiterite and occurs as massive to semi-massive lenses at the contact between the UNA Porphyry and meta-sandstone, and as veins and disseminated sulfides within the UNA Porphyry. The massive sulfide lenses are dominated by chalcopyrite

a	Minerals	Stage I (early)	→	Stage II (late)
	Quartz	—————		—————
	Sericite	—————		—————
	Biotite	—————		—————
	Muscovite	—————		—————
	Garnet	—————		—————
	Biotite	—————		—————
	Chlorite	—————		—————
	Magnetite	—————		—————
	Cassiterite	—————		—————
	Siderite			—————
	Fluorite			—————
	Pyrite		—————	
	Arsenopyrite			—————
	Stannite			—————
	Pyrrhotite		—————	
	Chalcopyrite		—————	
	Sphalerite		-----	
b	Minerals	Stage I (early)	→	Stage II (late)
	Quartz	—————		—————
	Sericite	—————		—————
	Rutile		—————	
	Siderite			-----
	Cassiterite	—————		—————
	Marcasite		—————	
	Sphalerite		—————	
	Galena		—————	
	Stannite			-----
	Chalcopyrite		-----	—————
	Pyrrhotite		-----	—————

**Fig. 3** Mineral paragenesis summary illustrations of **a** the Baal Gammon deposit; and **b** the Isabel deposit

and pyrrhotite and were mostly mined out. Locally, chalcopyrite from the massive sulfide lenses display oriented exsolution lamellae of pyrrhotite (Fig. 4c). Variable amounts of sphalerite, stannite, cassiterite, magnetite, and trace levels of galena and pyrite occur as inclusions in pyrrhotite and chalcopyrite. The semi-massive sulfide mineralization is commonly surrounded by a zone of intense stockwork micro-veining and alteration (Fig. 2c). The micro-veins are sulfide-rich and consist mainly of chalcopyrite and pyrrhotite. The zones of stockwork veining are generally intensely silicified (Fig. 2c). The stockwork veining and the

associated silicification appear to be better developed in the meta-sandstone. The chalcopyrite-pyrrhotite veins (Fig. 2b) have variable thickness, and crosscut the UNA Porphyry and meta-sandstone contact. Disseminated sulfide mineralization consists of medium-sized grains of chalcopyrite and pyrrhotite that form low-grade ore zones in the UNA Porphyry and the silicified meta-sandstone (silica-cap, Fig. 2a). Sphalerite occurs as inclusions of < 200- $\mu$ m-wide subhedral grains in chalcopyrite and pyrrhotite. Stannite occurs mainly in alteration zones around cassiterite grains (Fig. 4b) and as equant inclusions (~ 10–50  $\mu$ m wide) in chalcopyrite, pyrrhotite, and sphalerite. In massive sulfides, micrometer-sized stannite grains occur along grain boundaries and/or in microfractures in chalcopyrite, pyrrhotite, and sphalerite. Arsenopyrite occur as crosscutting veins and overprints the massive and semi-massive sulfides.

At the Isabel deposit, two mineralization stages (Fig. 3b) were recognized. Stage I consists of disseminated cassiterite grains, whereas stage II consists of massive sulfide veins comprising mainly of sphalerite, galena, and minor chalcopyrite and stannite. The cassiterite from stage I mineralization occurs as subhedral to euhedral grains that either form clusters or are randomly distributed in the hydrothermal breccia. In the massive sulfide veins, cassiterite occurs mainly as inclusions in sphalerite. No alteration of cassiterite to stannite was observed, although stannite grains are present in the samples with cassiterite.

The stage II massive sulfide veins can be separated into two distinct type of vein sets. The type I sulfide veins occur as 1 to 2 m wide, lenticular-shaped ore bodies that are oriented SW-NE and up to 10 m in length. They consist of coarse sphalerite grains with minor chalcopyrite inclusions (Fig. 4d) that are crosscut by ~ 1-cm-thick chalcopyrite veins (Fig. 4e) and by thin (~ 2 mm wide) chalcopyrite-pyrrhotite veins (Fig. 2d). The density of the crosscutting chalcopyrite-pyrrhotite veins is low and they are oriented parallel or at a low angle to the massive sphalerite veins. Type II sulfide veins consist of sphalerite and galena (Fig. 2f) and are 0.5 to 1 m wide. These veins have a similar orientation to the type I veins and are surrounded by coarse milky quartz grains that are variably fractured. The infill of these fractures consists mainly of galena, chalcopyrite, and pyrrhotite. Stannite occurs in association with sulfide veins and can be found as inclusions in sphalerite or as clusters of subhedral grains surrounding galena (Fig. 4f). Minor amounts of arsenopyrite, marcasite, and siderite are also associated with stage II mineralization (Fig. 3b).

### FE-EPMA spot analysis and compositional map results

A summary of the average compositions for different mineral phases from the Baal Gammon and Isabel deposits are presented in Tables 1 and 2, and the Supplementary information 2.

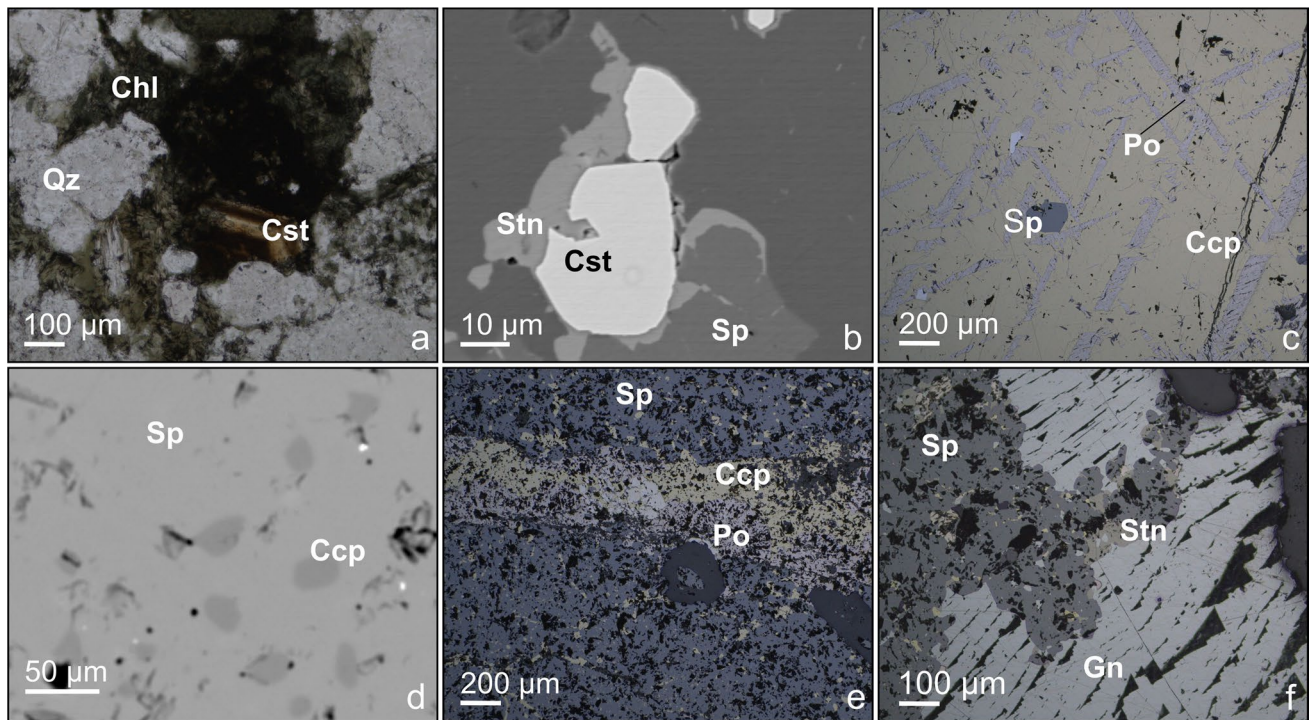


**Fig. 4** Reflected light (RL) and backscattered electron (BSE) images of ore at the Baal Gammon (a–c) and Isabel (d–f) deposits. **a** Cassiterite (Cst) surrounded by chlorite (Chl) and quartz (Qz) in the UNA porphyry. **b** BSE image showing alteration of cassiterite to stannite (Stn) in massive sulfides. **c** Pyrrhotite (Po) exsolution in chalcopyrite

(Ccp). **d** BSE image of chalcopyrite inclusions in sphalerite (Sp). **e** RL image of chalcopyrite and pyrrhotite veining in sphalerite. **f** RL image of stannite (olive green) occurrence at the contact of sphalerite (gray) and galena

**Sphalerite**

Of the two deposits, the Baal Gammon deposit shows greater variation in chemical composition of sphalerite than the Isabel deposit (Supplementary information 2; Fig. 5a), with Zn

ranging from 35.7 to 56.0 wt%, Fe from 9.45 to 16.3 wt%, Cu from 0.13 to 13.9 wt%, and In from 0.15 to 2.21 wt%. There is limited compositional variation for minor elements such as Cd (0.23 to 0.38 wt%), Sn (up to 0.31 wt%), and Ga (avg. 0.03 wt%). In comparison, the sphalerite from the

**Table 1** Average composition of ore minerals from the Baal Gammon deposit measured by FE-EPMA

	wt%(SD)	Arsenopyrite	Pyrrhotite	Chalcopyrite	Stannite	K�sterite	Sphalerite	Cassiterite
<i>n</i>	10	13	10	6	7	19	11	
S	19.8(0.2)	39.4(0.4)	34.4(0.1)	29.5(0.1)	31.8(0.4)	33.2(0.2)	bdl	
Cu	bdl	0.06(0.12)	33.4(0.3)	27.2(0.7)	10.3(1.4)	2.34(3.22)	0.26(0.13)	
As	44.7(0.4)	–	–	–	–	–	–	
Cd	bdl	bdl	bdl	bdl	0.27(0.04)	0.32(0.04)	bdl	
In	bdl	bdl	0.10(0.04)	0.82(0.75)	8.00(2.28)	0.68(0.61)	0.01(0.01)	
Sn	bdl	bdl	0.15(0.07)	26.6(1.0)	4.76(2.08)	0.04(0.08)	78.3(0.5)	
Pb	–	–	–	–	–	–	–	
Ag	bdl	bdl	0.04(0.04)	0.07(0.04)	bdl	bdl	bdl	
Ga	bdl	bdl	bdl	bdl	bdl	0.03(0.01)	–	
Fe	36.1(0.2)	61.0(0.6)	30.6(0.2)	13.0(0.4)	14.1(2.5)	11.3(1.5)	0.42(0.30)	
Zn	bdl	0.08(0.18)	0.16(0.18)	2.06(0.56)	31.3(4.6)	52.1(4.4)	0.07(0.12)	
Sb	0.05(0.05)	bdl	bdl	bdl	0.06(0.02)	bdl	–	
Co	0.07(0.14)	bdl	bdl	bdl	n.d	bdl	–	
O	na	na	na	na	na	na	21.3(0.2) <sup>1</sup>	
Total	100.7(0.4)	100.5(0.4)	98.8(0.3)	99.3(0.4)	100.6(1.1)	100.0(0.5)	100.3(0.8)	

<sup>1</sup>Oxygen calculated by stoichiometry

**Table 2** Average composition of galena, stannite, and sphalerite from the Isabel deposit measured by FE-EPMA

wt%(SD)	Galena	Stannite	Sphalerite
<i>n</i>	10	9	14
S	13.7(0.1)	29.5(0.1)	33.3(0.2)
Cu	bdl	27.6(0.1)	0.33(0.54)
Cd	–	bdl	0.29(0.03)
In	bdl	0.33(0.06)	0.11(0.05)
Sn	0.06(0.07)	27.0(0.1)	0.15(0.41)
Pb	86.0(0.3)	–	–
Ag	n.d	0.24(0.02)	n.d
Ga	–	bdl	0.04(0.01)
Fe	bdl	12.5(0.2)	10.1(0.82)
Zn	bdl	3.15(0.37)	55.9(1.6)
Sb	0.11(0.03)	bdl	bdl
Co	bdl	bdl	bdl
Total	99.9(0.3)	100.4(0.4)	100.2(0.1)

Isabel deposit (Table 2; Fig. 5a) is less variable in Zn (52.4 to 57.4 wt%) and Fe (8.94 to 11.5 wt%), and shows lower concentrations and variability in Cu (0.03 to 1.60 wt%) and In (0.06 to 0.18 wt%). The minor element concentrations in sphalerite from the Isabel deposit are similar to those from Baal Gammon, except for Sn, where two analyses yield anomalous values (0.79 and 1.37 wt%) that likely reflect interception of cassiterite and or stannite inclusions (Supplementary information 2).

Sphalerite mineral compositions from the Baal Gammon deposit are summarized in Table 1 and Fig. 5. The concentration of In varies systematically with the concentration of Cu (Fig. 5c) but systematic variation is not observed of In with Fe, Zn, Cd, or Ga (Fig. 6). The observed chemical heterogeneity is due partly to variations among individual grains and partly to compositional zoning as revealed by EPMA maps (Fig. 8). The highest In and Cu concentrations are present in sphalerite rims (Fig. 8) and in small sphalerite grains found along the grain boundaries between sphalerite, and chalcopyrite and pyrrhotite (Fig. 9). However, in general, the compositional difference between the core and rim of a sphalerite grain is less than that observed among different grains. The core of some sphalerite grains has 0.28 wt% In and 2.18 wt% Cu whereas the rim has 0.92 wt% In and 2.44 wt% Cu (Fig. 8b). In contrast, some smaller sphalerite grains have up to 2.21 wt% In (Fig. 9). Copper shows the largest compositional variation in sphalerite from Baal Gammon ranging from 0.13 to 13.9 wt% (Table 1). EPMA compositional maps (Fig. 8c) indicate that high Cu-rich areas in sphalerite have a spotty appearance suggesting that Cu occurs as micron to submicron inclusions of chalcopyrite. This implies that a few high Cu concentrations represent mixed sphalerite

and chalcopyrite analyses and In/Cu ratio from these zones are less than one (Fig. 5(c)). On a ternary diagram (Fig. 5a), the composition of these sphalerite grains plots towards chalcopyrite rather than stannite as is typical for In-rich natural sphalerite. The EPMA compositional maps of sphalerite grains from the Isabel deposit (Fig. 10) are consistent with the spot analyses (Table 2). They show limited compositional variation on the ternary diagram (Fig. 5a) and plot near the sphalerite composition and most analyses have an In/Cu ratio of close to one (Fig. 5c).

### Stannite-k esterite

The stannite group minerals include stannite and k esterite at Baal Gammon and stannite at Isabel (Table 1 and 2; Fig. 5b). Stannite from both deposits has similar major element compositions in near end-members from the group (within ~ 1 wt% for S, < 4% for Sn and Fe, and < 8% for Cu) with wt% averages within error of one another for these elements. Significant differences exist in In variability and content ( $0.82 \pm 0.75$  vs.  $0.33 \pm 0.06$  wt% at Baal Gammon and Isabel respectively), and in the content of Ag ( $0.07 \pm 0.04$  vs.  $0.24 \pm 0.02$  wt%) and Zn ( $2.06 \pm 0.56$  vs.  $3.15 \pm 0.37$  wt%). The composition of k esterite from Baal Gammon is highly variable and indicates a transition from stannite to ferrok esterite (Fig. 5a, b). There are large compositional variations for all major elements including Cu (8.03 to 12.7 wt%), In (4.36 to 10.6wt%), Sn (1.79 to 7.52 wt%), Fe (12.5 to 18.9 wt%), and Zn (24.5 to 36.8 wt%). Minor amounts of Cd (avg. 0.27 wt%) and trace amounts of Ag (0.03 wt%) and Sb (0.06 wt%) are also found in k esterite.

### Chalcopyrite, pyrrhotite, arsenopyrite, and galena

Chalcopyrite, pyrrhotite, and arsenopyrite grains were analyzed for the Baal Gammon deposit and galena for the Isabel deposit. These phases are homogeneous for major element compositions (Table 1). Minor to trace amounts of In (0.08 to 0.19 wt%), Sn (0.07 to 0.27 wt%), Ag (up to 0.11 wt%), and Zn (0.06 to 0.66 wt%) are common in chalcopyrite grains (Table 1; Supplementary information 2). In chalcopyrite, In does not correlate with any other elements (Fig. 7c–d). The pyrrhotite grains are homogeneous and contain 39.4 wt% S and 61.0 wt% Fe ( $\text{Fe}_{0.89}\text{S}$ ). Minor amounts of Cu (up to 0.36 wt%) and Zn (up to 0.67 wt%) and trace amounts of Sn (up to 0.07 wt%) and Co (up to 0.03 wt%) are present in pyrrhotite. Arsenopyrite is non-stoichiometric ( $\text{Fe}_{1.04}\text{As}_{0.96}\text{S}$ ) and contains trace quantities of Cu, Sn, Sb, and Co. Indium is below the detection limit in pyrrhotite and arsenopyrite. Galena from the Isabel deposit contains minor amounts of Sn (up to 0.16 wt%), Sb (avg. 0.11 wt%), and Ag (0.10 wt%), and In is below the detection limit (Table 2).



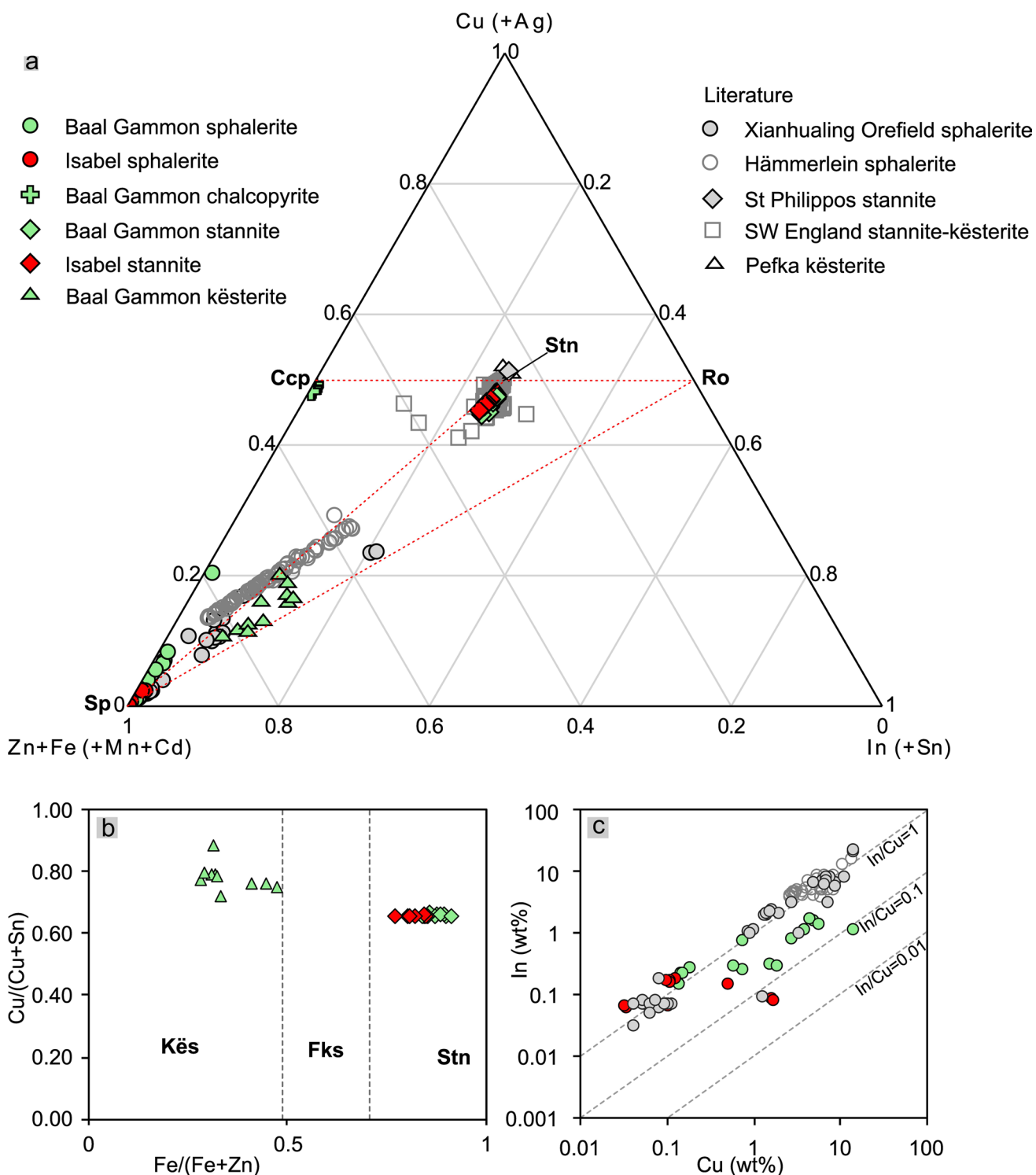


**Fig. 5** **a** Ternary plot (atomic proportions) for sphalerite, chalcopyrite, stannite, and kesterite from the Baal Gammon deposit, Isabel deposit, Xianhualing Orefield (Liu et al. 2017), Hämmerlein skarn deposits (Bauer et al. 2019b), St. Philippos and Pefka deposits (Voudouris et al. 2022), and the deposits from SW England (Andersen

et al. 2016). **b** Stability field of stannite group minerals based on element composition in atomic proportions as a function of Cu/(Cu+Sn) vs. Fe/(Fe+Zn). **c** Binary plot of sphalerite showing variation in Cu and In

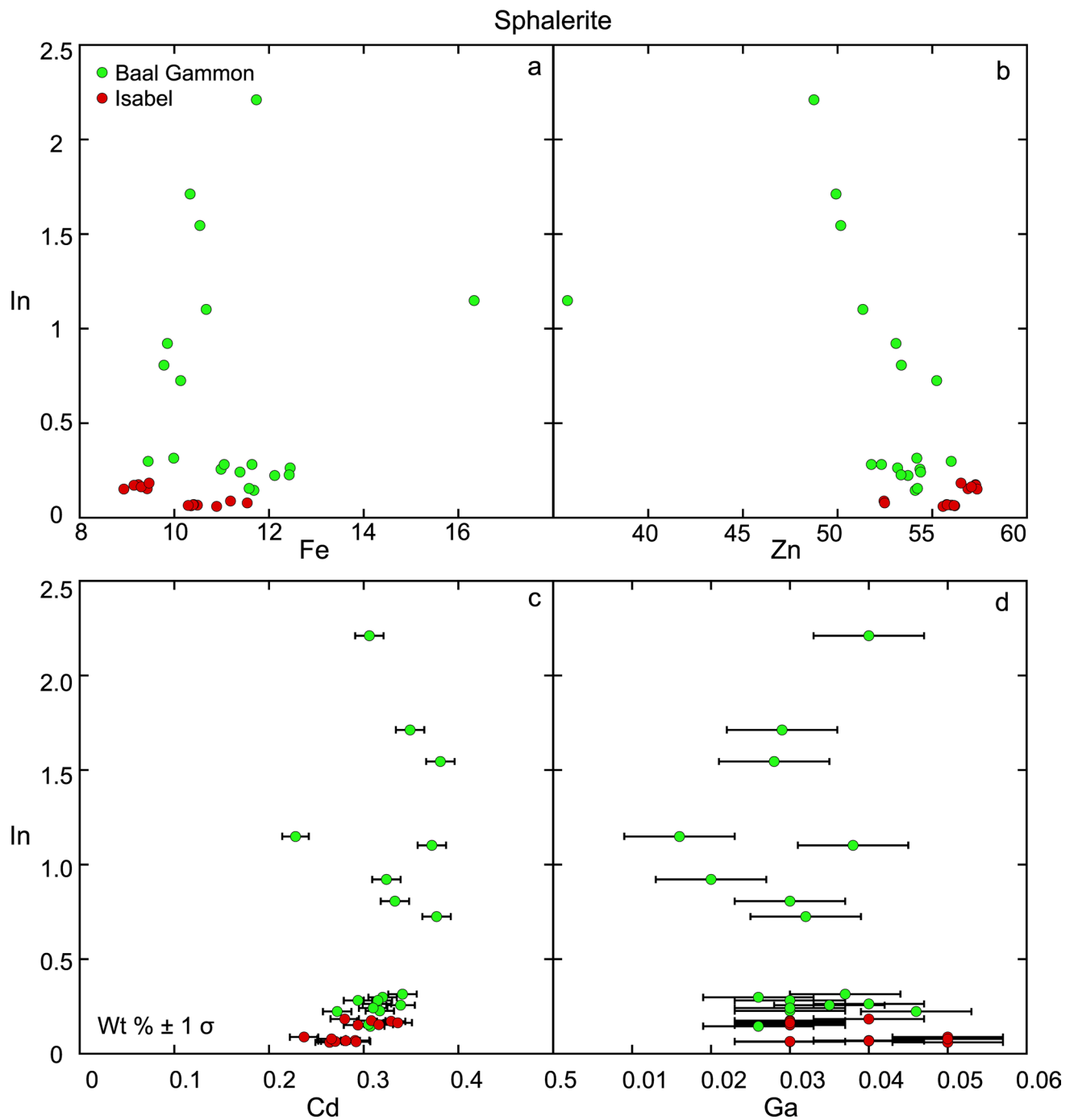


**Fig. 6** Indium vs Fe, Zn, Cd, and Ga in sphalerite (element wt%) in the Baal Gammon and Isabel deposits. Analytical error ( $\pm 1\sigma$ ) is within symbol size for In, Fe, and Zn

### Element distribution maps

EPMA compositional maps of the Baal Gammon deposit indicate that In is concentrated along the rims of sphalerite grains in chalcopyrite and pyrrhotite (Figs. 8 and 9). High-resolution compositional maps indicate high In

concentrations in sphalerite along narrow rims at sphalerite, chalcopyrite, and pyrrhotite contact (Fig. 9b). Locally, Sn-rich phases such as stannite and k esterite are present (Figs. 8 and 9) at contact between chalcopyrite, sphalerite, and pyrrhotite grains, but commonly appear as inclusions within the pyrrhotite grains (Fig. 8d). The microfractures that crosscut

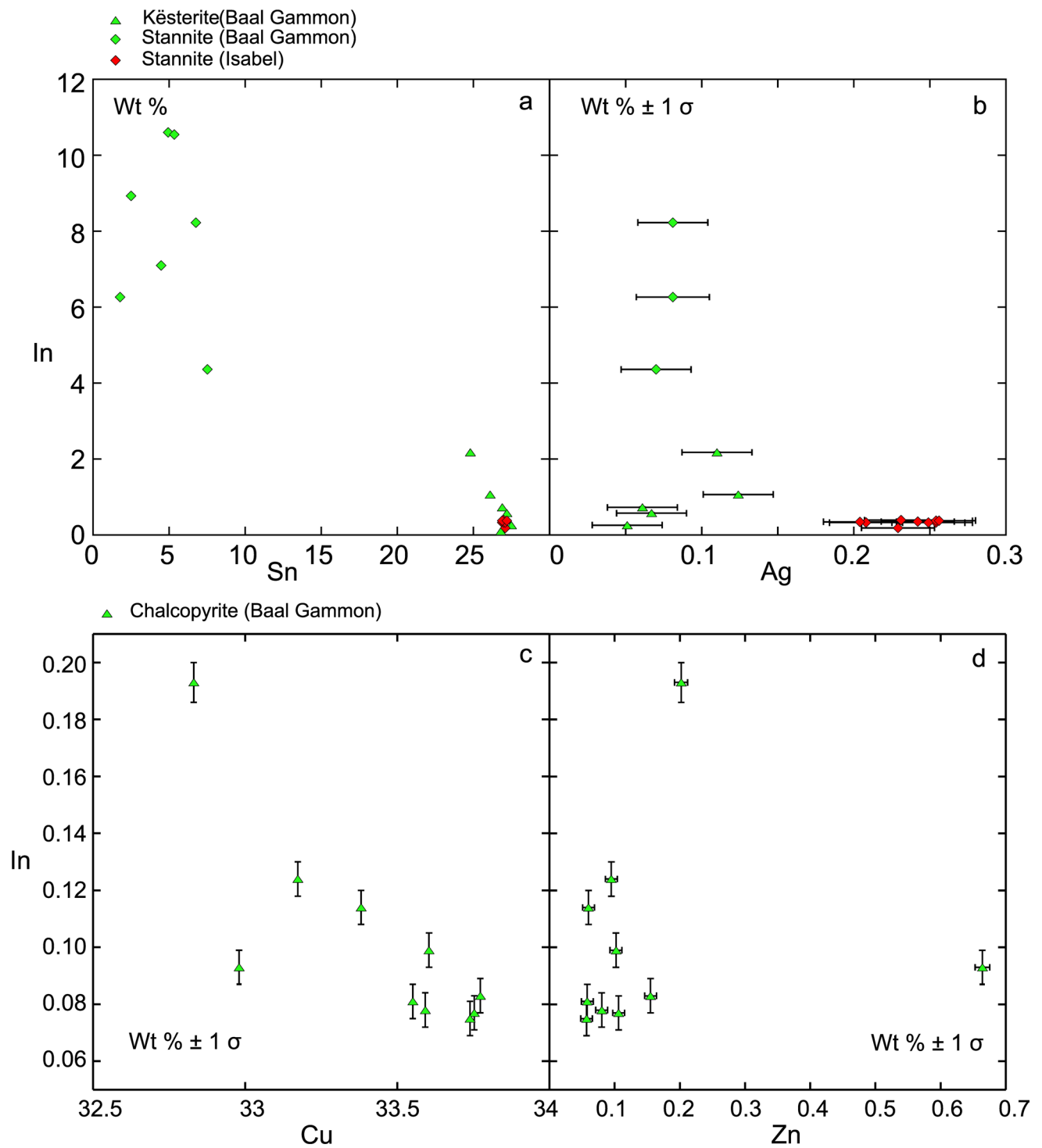


**Fig. 7** Compositional variation (element wt %) of In in **a–b** stannite group minerals, and **c–d** chalcopyrite. Analytical error ( $\pm 1\sigma$ ) is within symbol size for In and Sn

the sulfide grains do not appear to be related to In enrichment in the neighboring grains or in the In-rich phases. In the Isabel deposit, In distribution is relatively homogenous within individual sphalerite grains (Fig. 10) but variations

occur between different grains and between sphalerite grains from different samples (Fig. 4d–f). No detectable compositional variations were measured in the adjacent stannite grains present in type II veins (Figs. 4f and 10).

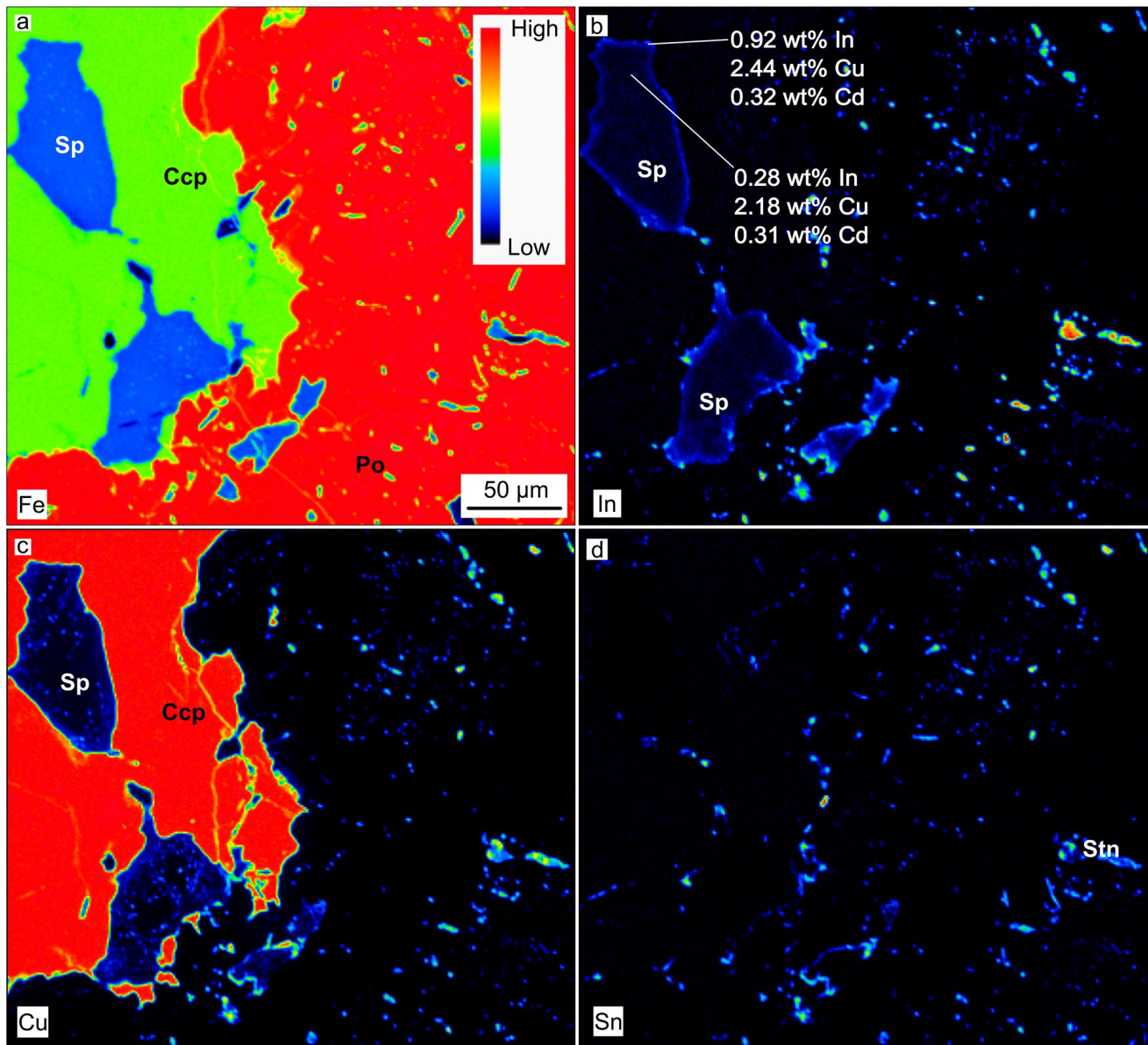


**Fig. 8** EPMA-WDS background-corrected stage maps showing distribution of Fe, In, Cu, and Sn in massive sulfides from the Baal Gammon deposit

### Eh, pH, and In chlorine complex modeling results

The results obtained from geochemical modeling is presented in Fig. 13. The pH vs. temperature plot shows that favorable hydrothermal condition for  $\text{InCl}^{++}$  complex is a low pH ( $\sim 3$ ) at  $\sim 300^\circ\text{C}$ . Modeling of the ore minerals confirms that the In-rich assemblages of chalcopyrite, pyrrhotite, and sphalerite, observed at the Baal Gammon and Isabel deposits, formed at low pH ( $\sim 3$ ) and under reduced conditions.

### Discussion

#### Timing and distribution of indium in sulfide ores at the Baal Gammon and Isabel deposits

The sulfide phases that contain significant In are sphalerite, stannite, k esterite, and chalcopyrite in the Baal Gammon deposit (Table 1), and sphalerite and stannite in the Isabel deposit (Table 2). Cassiterite from the Baal Gammon deposit contains minor amounts of In. The mineral

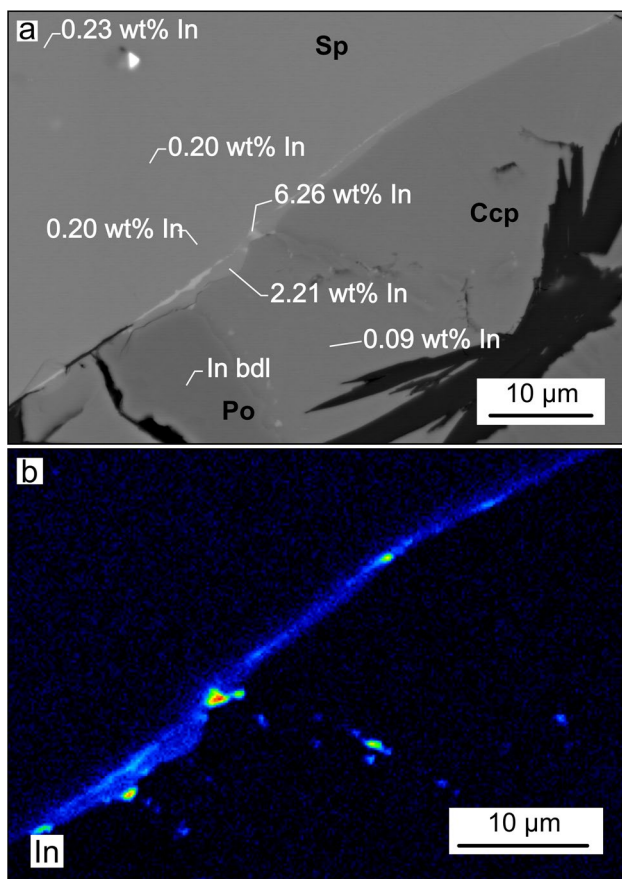


**Fig. 9** **a** Backscattered electron (BSE) image of massive sulfide from the Baal Gammon deposit, and **b** corresponding background-corrected EPMA-WDS map (beam scan) of relative In La X-ray intensities in the different phases showing In-rich zones along the grain boundary of chalcopyrite (Ccp) and sphalerite (Sp). Conditions for mapping were 6-kV accelerating voltage, 60-nA beam current, and fully focused beam to yield spatial resolution of ~170 nm per pixel

paragenesis (Fig. 3) at both deposits show cassiterite predating sulfide mineralization. At the Baal Gammon deposit, cassiterite grains are partly to completely replaced by stannite and k esterite (Fig. 4b), whereas in the Isabel deposit the cassiterite grains are unaltered, although stannite is a common mineral phase. This may indicate that the Sn needed to form stannite at the Isabel deposit was either introduced with the sulfides or derived by the dissolution of stage I cassiterite grains. The irregular boundaries between stannite and sphalerite grains (Fig. 4f) at the Isabel deposit indicate co-genetic minerals phase. The chalcopyrite and pyrrhotite at the Isabel deposit occur as fine-grained inclusions in sphalerite and as crosscutting veinlets. This indicates that initially some chalcopyrite and pyrrhotite co-crystallized with the sphalerite and stannite. Since chalcopyrite and pyrrhotite are only minor phases at the Isabel deposit, the main hosts for In are sphalerite and stannite. EPMA compositional mapping indicates that

In is homogeneously distributed in sphalerite and stannite (Fig. 10). This is supported by restricted compositional variation in the spot analyses (Table 2; Fig. 5) and indicates that In was synchronously introduced and incorporated into the crystal structure of stannite at Isabel with the stage II sulfide ores.

The main sulfide phases at Baal Gammon include chalcopyrite followed by pyrrhotite, small amounts of sphalerite, stannite, k esterite, and minor amounts of pyrite. Pyrite predates sulfide mineralization and is rare within the ore zones. Arsenopyrite occurs as late crosscutting veins that locally overprint the earlier sulfide phases (Fig. 3). The presence of pyrrhotite exsolutions surrounding chalcopyrite (Fig. 4c) indicates that these phases exsolved from a sulfide solid solution. Sphalerite occurs mainly as inclusions in chalcopyrite and pyrrhotite. The presence of minute inclusions of chalcopyrite in sphalerite rims (Fig. 8c) suggests that sphalerite co-precipitated with the chalcopyrite and pyrrhotite. Direct replacement of cassiterite by stannite and inclusions of k esterite within chalcopyrite and pyrrhotite are consistent with the formation of stannite and k esterite with chalcopyrite, pyrrhotite, and sphalerite. EPMA compositional mapping (Figs. 8 and 9) reveals that In is homogeneously distributed within chalcopyrite grains, but is enriched in the rims of sphalerite grains in contact with chalcopyrite and/or pyrrhotite. The lack of crosscutting fractures and the fact that most sphalerite grains are included in chalcopyrite and/or pyrrhotite indicate that the In enrichment along the sphalerite rims is likely a primary feature related to the initial crystallization of the sulfide ores.

### In and Cu incorporation in sphalerite

Indium incorporation in sphalerite occurs by coupled substitution of  $\text{In}^{3+}$  and  $\text{Cu}^+$  for two  $\text{Zn}^{2+}$  cations (e.g., Johan 1988; Cook et al. 2009, 2012; Andersen et al. 2016; Torr o et al. 2019a, b; Xu et al. 2021). This substitution indicates that the incorporation of In into the sphalerite structure occurs at a 1:1 ratio with Cu, and the In–Cu bearing natural sphalerite represents a solid solution crystallized in a cubic sphalerite structure (e.g., Schorr and Wagner 2005; Schorr et al. 2006). EPMA analyses of sphalerite from the Baal Gammon and Isabel deposits indicate that most sphalerite analyses from the Baal Gammon deposit deviate from the expected  $\text{Cu}/\text{In} = 1$  ratio, whereas most of the sphalerite grains from the Isabel deposit plot close to the expected  $\text{Cu}/\text{In} = 1$  ratio (Fig. 5c). The deviation from the expected  $\text{Cu}/\text{In} = 1$  ratio is best explained by the presence of chalcopyrite micro-inclusions in sphalerite as indicated by EPMA compositional mapping (Fig. 8 c). A compilation of EPMA analyses of In-bearing sphalerite grains from the literature (Fig. 11) indicates that the molar  $\text{Cu}/\text{In}$  ratio of most natural sphalerite is less than

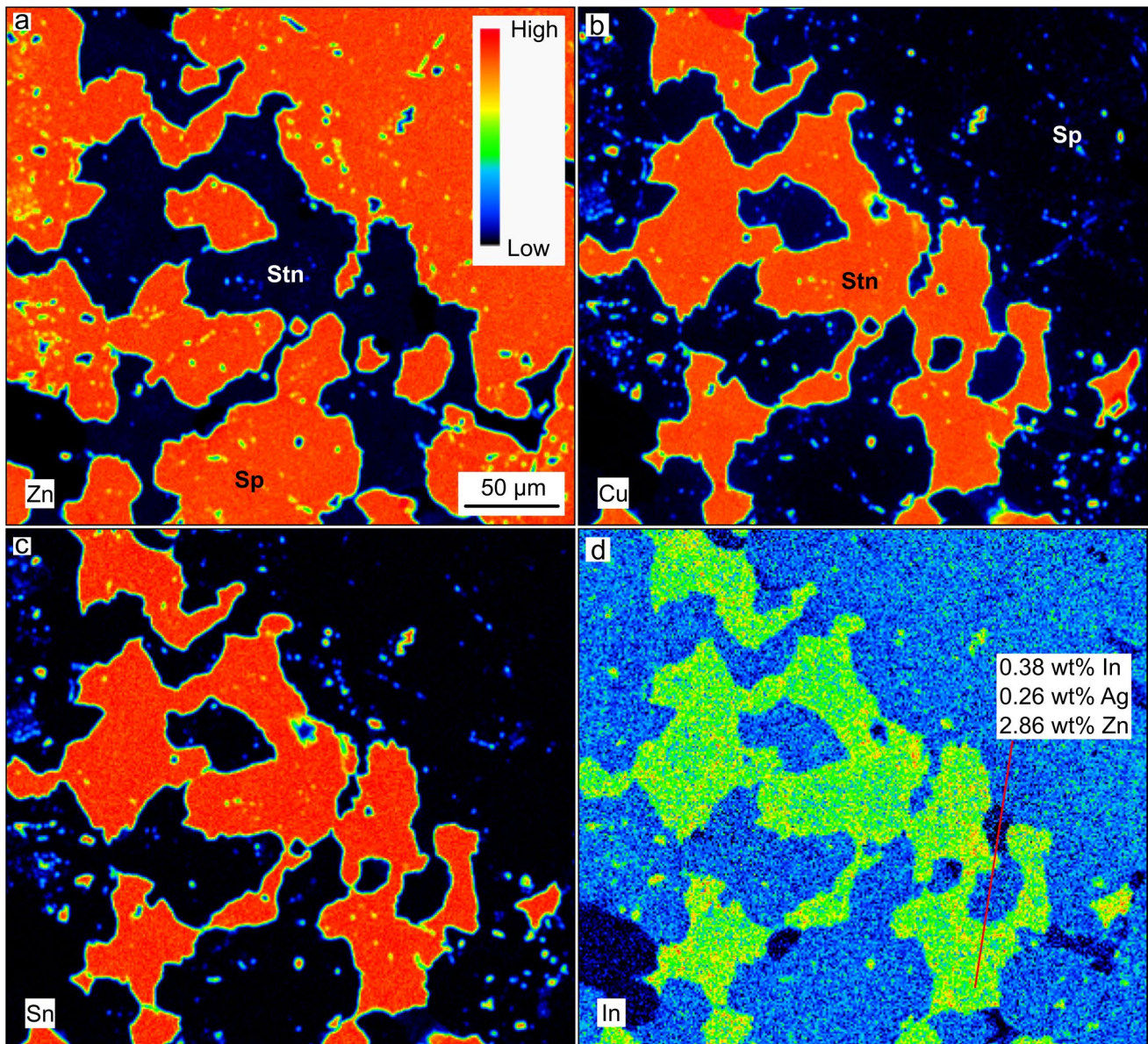


**Fig. 10** Background-corrected EPMA-WDS stage maps showing distribution of Zn, Cu, Sn, and In in type 1 sphalerite veins from the Isabel deposit. Conditions for mapping were 15-kV accelerating voltage, 60-nA beam current, and 1-micron step size (=defocused beam diameter)

1, suggesting that there is almost always an excess of Cu compared to In. Experimental results for the Cu–Fe–Zn–S system (Wiggins and Craig 1980; Hutchison and Scott 1981; Kojima and Sugaki 1985) indicate that the solubility of Cu in sphalerite is limited under low-temperature hydrothermal conditions, which is in agreement with our findings. It suggests that the high Cu analyses represent chalcopyrite micro-inclusions rather than high Cu contents in the sphalerite structure. The analyses plotted above the Cu/In = 1 ratio (Fig. 11) may indicate the presence of micro-inclusions of In-rich mineral phases such as roquesite. Moreover, the operation of complex solid solutions (Fig. 5a)

between sphalerite and stannite, sphalerite and  $\text{CuZn}_2\text{InS}_4$ , chalcopyrite and stannite, and roquesite and  $\text{CuZn}_2\text{InS}_4$  can complicate the chemical distribution of In between co-existing phases. All sphalerite analyses from the Baal Gammon and Isabel deposits plot near the sphalerite end-member on the ternary plot (Fig. 5a) or along the sphalerite to chalcopyrite tie line in accordance with the presence of chalcopyrite inclusions in sphalerite. None of the sphalerite analyses plot along the tie lines for stannite, k esterite, and roquesite compositions (Fig. 5a), suggesting that none of the mentioned solid solutions are found in sphalerite from the Baal Gammon and Isabel deposits.

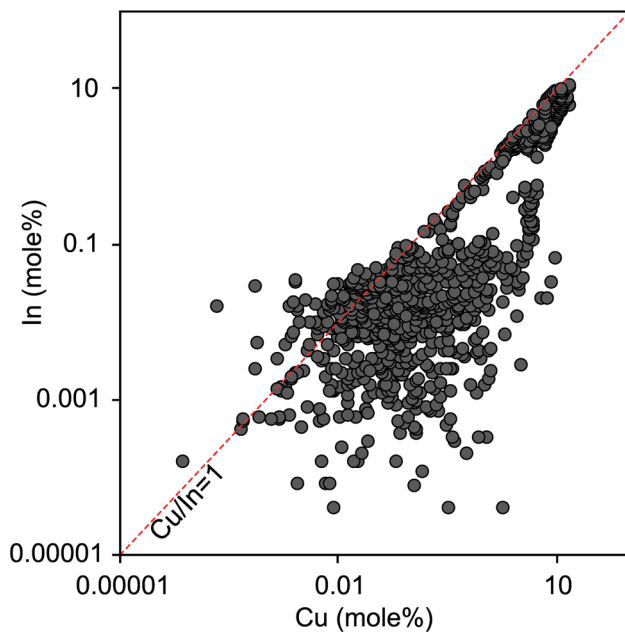


**Fig. 11** Log (Cu)-log (In) plot of sphalerite data compiled from the literature and including this study, showing two fields; one below the Cu/In=1 line in a wedge shape; and the other above the Cu/In=1 line. The Cu/In=1 divide represents the maximum solubility of In in sphalerite. Sphalerite composition from this study was combined with data from Andersen et al (2016), Liu et al (2017), Bauer et al (2019b), and Xu et al (2021) for the plot. Data that plot above the Cu/In=1 line are interpreted as possible In-rich micro-inclusions based on observations in this study

### Stannite-sphalerite thermometer and the temperature of ore formation

Experimental work shows that the partitioning of Fe and Zn between co-existing sphalerite and stannite is temperature-dependent, and that the Fe and Zn content of co-existing sphalerite and stannite can be used to calculate the equilibrium temperature of crystallization for this mineral pair (Nekrasov et al. 1979; Shimizu and Shikazono 1985). The Baal Gammon and Isabel deposits contain sphalerite-stannite mineral pairs which are likely co-genetic, as discussed above. The Fe and Zn partitioning between sphalerite-stannite mineral pair can be described by the following reaction:



Equation (1) describes the solid solution reaction between stannite and sphalerite, where the k esterite end-member of the stannite group mineral formed as ZnS is replaced by FeS from the sphalerite solid solution series. The equilibrium temperature for sphalerite-stannite mineral pairs can be described by the following equations:

$$T(^{\circ}\text{C}) = 1274/(\log K_D) - 273 \quad (\text{Nekrasov et al. 1979}) \quad (2)$$

$$T(^{\circ}\text{C}) = 2800/(3.5 - \log K_D) - 273 \quad (\text{Shimizu and Shikazono 1985}) \quad (3)$$

where,

$$K_D = (\text{Fe/Zn})_{\text{sphalerite}}/(\text{Fe/Zn})_{\text{stannite}}$$

Comparison between temperatures obtained by the above equations and fluid inclusions and isotope geothermometry indicates that Eq. (3) yields temperatures that are in agreement with those obtained from fluid inclusion and isotope geothermometry, whereas Eq. (2) consistently returns lower values (e.g., Shimizu and Shikazono 1985; Brill 1989; Sinclair et al. 2006). Therefore, we used Eq. (3) to calculate the equilibrium temperature of co-existing sphalerite and stannite.

The Fe content of sphalerite from Baal Gammon varies between 9.45 and 16.3 wt% and the Zn content varies between 35.7 and 56.0 wt%, whereas the Fe content of stannite varies between 12.3 and 13.5 wt%, and the Zn content between 1.40 and 2.74 wt%. The corresponding equilibration temperature based on Eq. (3) varies from 269 to 305  $^{\circ}\text{C}$  with an average value of  $290 \pm 12$   $^{\circ}\text{C}$ . The Fe content of sphalerite from the Isabel deposit varies from 8.94 to 11.5 wt% and the Zn content varies between 52.4 and 57.4 wt%, whereas the Fe content of stannite varies between 12.1 and 12.6 wt% and the Zn content between 2.61 and 4.35 wt%. The corresponding equilibration temperature based on Eq. (3) varies from 291 to 321  $^{\circ}\text{C}$  with an average value of  $307 \pm 9$   $^{\circ}\text{C}$ . Since sphalerite (avg. In of 0.68 and 0.11 wt% at Baal Gammon and Isabel respectively) and stannite (avg. In of 0.82 and 0.33 wt%), including k esterite end-member, contain the highest In content (Tables 1 and 2), and formed synchronous with chalcopyrite, we interpret sphalerite-stannite thermometer results as the temperature of formation for In mineralization in the Baal Gammon and Isabel deposits.

### Indium in relation to the Cu–Fe–Zn–S system and sulfide precipitation in the Baal Gammon deposit

The Baal Gammon mineral paragenesis indicates that chalcopyrite, pyrrhotite, and sphalerite are co-genetic (Figs. 3 and 4). Moreover, the presence of pyrrhotite exsolution in chalcopyrite (Fig. 4c) infers the existence of a Cu-rich intermediate solid solution (iss) during sulfide ore deposition as described by a series of experiments under hydrothermal conditions in the Cu–Fe–Zn–S system at temperatures between 300 and 500  $^{\circ}\text{C}$  (Sugaki et al. 1975, 1982; Kojima and Sugaki 1985). The sphalerite-stannite thermometer gave a temperature of  $\sim 290$   $^{\circ}\text{C}$  likely for ore formation in the Baal Gammon deposit. At 300  $^{\circ}\text{C}$ , the assemblages chalcopyrite + pyrite + pyrrhotite + sphalerite

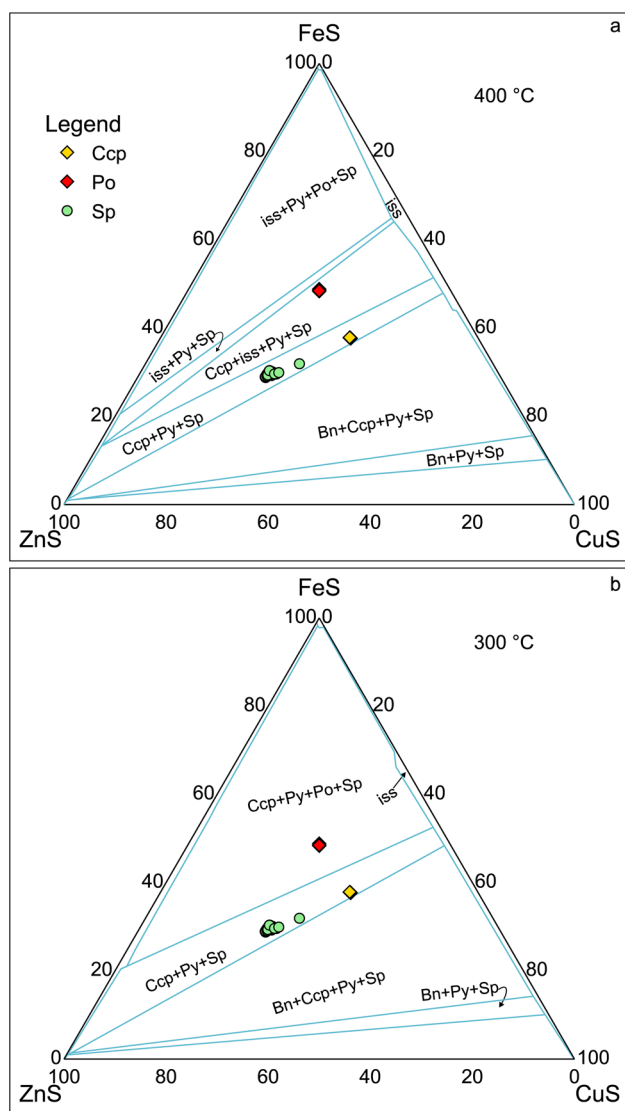


**Fig. 12** Ternary plot for Cu–Fe–Zn–S system at **a** 400 °C and **b** 300 °C, with phase relationships modified from Kojima and Sugaki (1985). FE-EPMA results of chalcopyrite (Ccp), pyrrhotite (Po), and sphalerite (Sp) from the Baal Gammon and Isabel deposits are plotted as atomic%; and other included phases are bornite (Bn), pyrite (Py), and intermediate solid solution (iss)

and chalcopyrite + iss + pyrrhotite + sphalerite (Fig. 12) occur according to the experimental results of Kojima and Sugaki (1985). Pyrite is rare in the Baal Gammon deposit and textural evidence suggest it predated the stage II sulfide mineralization; therefore, only the later mineral assemblage occurs in the ores. At 400 and 500 °C, a tie line exists between the intermediate solid solution and pyrite, but at temperatures below 325 °C a tie line between chalcopyrite and pyrrhotite is stable (Sugaki et al. 1982). Thus, as the temperature drops below 325 °C, the iss with a cubanite ( $\text{CuFe}_2\text{S}_3$ ) intermediate composition (Sugaki et al. 1975) separates into chalcopyrite ( $\text{CuFeS}_2$ ) and pyrrhotite ( $\text{FeS}$ ; Fig. 4c). The presence of

well-developed exsolution lamellae of pyrrhotite from chalcopyrite (Fig. 4c) at the Baal Gammon deposit indicates the presence of the cubanite intermediate solid solution and puts further constraints on the temperature of ore formation to below 325 °C. The maximum solubility of Zn in chalcopyrite at 500 °C is 0.9 atomic% and at 300 °C is 0.6 atomic%, whereas the intermediate solid solution in equilibrium with sphalerite contains up to 3.3 atomic% Zn at 500 °C and up to 1.2 atomic% Zn at 300 °C (Kojima and Sugaki 1985). The intermediate solid solution with a composition close to that of cubanite dissolves slightly more Zn. These values suggest that with cooling, significant amounts of sphalerite can be exsolved from the iss. Sphalerite is not a major phase at Baal Gammon, and sphalerite grains commonly occur as small inclusions in the presence of pyrrhotite exsolution lamellae in chalcopyrite, suggesting that they were exsolved from the iss. Thus, petrographic analysis suggests that in the Baal Gammon deposit, chalcopyrite, pyrrhotite, and sphalerite precipitated from the hydrothermal fluid, and also exsolved from an iss of cubanite composition.

Apart from the hydrothermal solution, significant amounts of In could have been also present in the iss and that was incorporated in chalcopyrite, pyrrhotite, and sphalerite during exsolution. Since pyrrhotite is not a host for In, it is possible that a small In excess was created during pyrrhotite exsolution which accumulated as enrichment in sphalerite rims (Figs. 8 and 9b) in contact with chalcopyrite and pyrrhotite. While this is plausible, further work is needed to test this hypothesis.

### Physiochemical conditions for indium transport and deposition in hydrothermal environments

The stannite-sphalerite geothermometer and the presence of exsolutions of pyrrhotite and chalcopyrite (Fig. 4b) indicate that the sulfide mineralization occurred at ~300 °C. Indium is likely transported as chlorine complexes at this temperature in hydrothermal environments (Seward et al. 2000; Wood and Samson 2006). Majority of In chlorine complexes in solvation experiments occur as  $\text{InCl}_4^-$  (> 95% concentration; Seward et al. 2000) which are unstable unless the chlorine concentration (8 M) is very high (Schuffe et al. 1951; Wood and Samson 2006). Fluid inclusion studies at the Sn–Zn–In deposit in Hämmerlein, Germany (Korges et al. 2020; Bauer et al. 2019b), and the In–Au–Cu–Zn–Pb–Ag deposit in San Roque, Argentina (Dill et al. 2013), indicate low salinities (< 7 wt% NaCl eq); therefore, chlorine concentrations in the mineralizing fluids were low which likely favored  $\text{InCl}^{2+}$  formation. Korges et al. (2020) measured > 3000 ppm of Pb, Mn, and Zn in fluid inclusions from Sn–Zn–In deposit at Hämmerlein. Other cations such as Cu, Zn, and Pb present in higher concentrations will compete for chlorine which may further support the formation of  $\text{InCl}^{2+}$



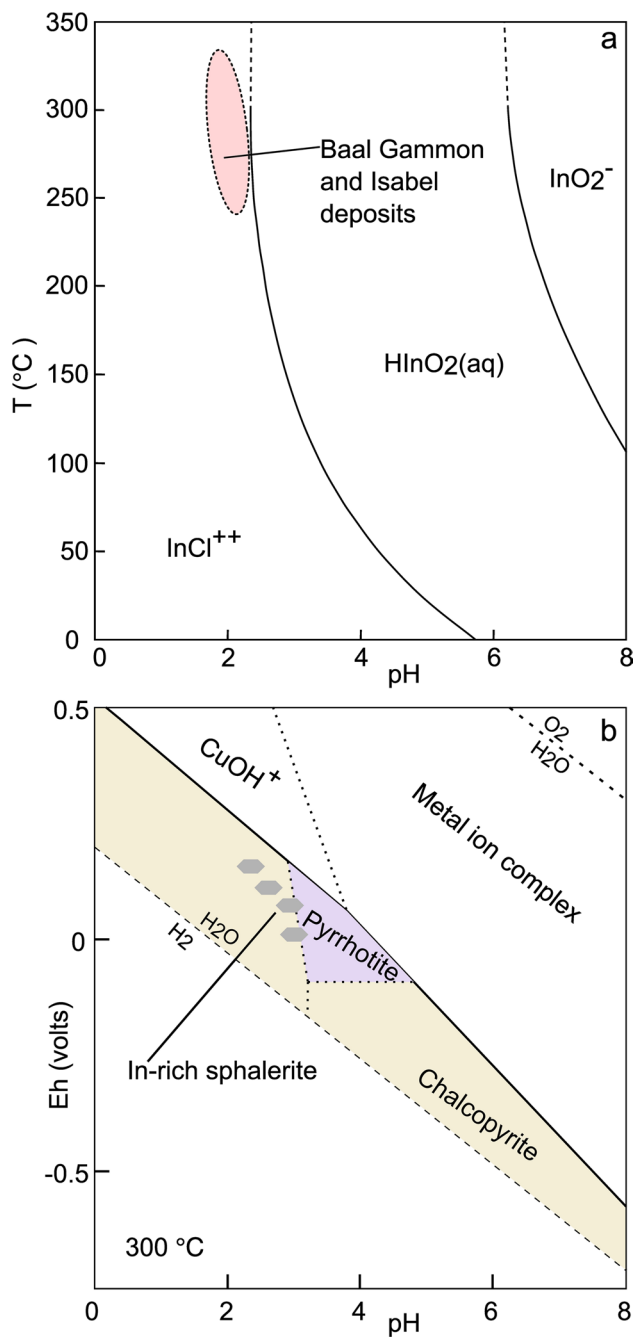


**Fig. 13** **a** Stability field plot of In-chlorine complex from 0 to 350 °C and a pH range of 0 to 8. The potential physio-chemical zone for Baal Gammon and Isabel deposits is estimated from the temperature range calculated through sphalerite-stannite geothermometer. The In–Cl temperature vs. pH decay plot is calculated using The Geochemist’s Workbench (Bethke et al. 2022) software with conditions:  $[In^{3+}] = 10^{-5}$ ,  $[Cl] = 10^{-1}$ , pressure = 1 bar, and  $H_2O$  at unity. **b** Eh–pH plot of sulfide assemblage present at the Baal Gammon and Isabel deposits. The Eh–pH plot was generated in The Geochemist’s Workbench (Bethke et al. 2022) software with configurations:  $[SO_4^{2-}] = 10^{-2}$ ,  $[Fe^{2+}] = 10^{-3}$ ,  $[Cu^+] = 10^{-3}$ , pressure = 1 bar, temperature = 300 °C, and  $H_2O$  at unity

over  $InCl_4^-$  in natural hydrothermal systems. Our geochemical modeling (Fig. 13a) indicates that  $InCl^{2+}$  is stable under acidic ( $pH < 3$ ) conditions at  $\sim 300$  °C. With increasing pH, other In species, such as  $HInO_{2(aq)}$  and  $InO_2^-$  (Fig. 13a), become stable. Similar physiochemical conditions likely favor incorporation of In in chalcopyrite and sphalerite. Our geochemical modeling of In-rich sulfide minerals (Fig. 13b) indicates that chalcopyrite and pyrrhotite in the Baal Gammon Sn–Cu deposit formed in reduced conditions at  $\sim 300$  °C and  $pH < 4$ .

Temperature ranges between 300 and 400 °C were observed for base-metal sulfide with In mineralization in other Sn fields, such as the Bolivian Sn belt (Lehmann 2020; Torres et al. 2019); the Freiberg Sn deposits, Germany (Bauer et al. 2019b, a; Korges et al. 2020); and the Xianghualing Sn field, China (Li et al. 2023). This indicates that favorable mineralizing conditions for In in Sn-polymetallic systems are below 400 °C with reduced, and acidic hydrothermal systems. Removal of In from solution is linked to sulfide precipitation and destabilization of In chlorine complexes. Similar mineralizing conditions to those inferred from the current study have been reported for other In-rich polymetallic systems where a direct connection to magmatism has been documented (Seifert and Sandmann 2006). Chlorine- and fluorine-rich fluids generated during granitic magmatism provide the ligands for  $In^{3+}$  ions to form complexes that enable hydrothermal transport and cycling during In mineralization.

Indium mineralization in the HMF is distributed mostly along the margins of granitic intrusions (Fig. 1), which suggests a genetic connection. At the Baal Gammon and Isabel deposits, porphyry dykes dated at  $\sim 290$  Ma (Kumar et al. 2022) display embayment textures that indicate magmatic-hydrothermal transition and exsolution of magmatic volatiles linked to mineralization (Kumar et al. 2022). These porphyry dykes together with the coeval granites were emplaced at the end of a post-collisional magmatic episode during a period of crustal thinning and relaxation (Champion and Bultitude 2013; Cheng et al. 2018). These late-stage felsic and rhyolitic granites are enriched in volatiles such as Cl and F (Bailey et al. 1982; Cheng et al. 2018) and thus constitute good sources of ligands for metals such as Cu, Zn, Pb, and In.

## Conclusions

In the Baal Gammon and Isabel deposits, two paragenetic stages have been recognized. The first stage consisted of cassiterite and did not host significant In. The second stage consisted of sulfides enriched in In. In the Baal Gammon deposit, In enrichment is observed in sphalerite, stannite,

chalcopyrite, and k esterite, while in the Isabel deposit only sphalerite and stannite are enriched. The stannite group minerals, such as k esterite, occur as alteration products of cassiterite, and they record the highest In (10.6 wt%) content. Ore textures at the Baal Gammon deposit indicate multiple processes, such as primary hydrothermal mineralization and exsolution of sulfides from intermediate phases, that concentrated In in the ores during deposition. The stannite-sphalerite thermometer gives average sulfide mineralization temperatures of 290  C for the Baal Gammon and 307  C for the Isabel deposits. These temperatures combined with the major sulfide assemblage and the physicochemical modeling indicates ore deposition in reduced and acidic (pH < 3) conditions.

**Supplementary Information** The online version contains supplementary material available at <https://doi.org/10.1007/s00126-023-01179-7>.

**Acknowledgements** This research was supported by the Geological Survey of Queensland under the New Economy Minerals Initiative and AAK was supported by a Commonwealth Research scholarship at James Cook University. We thank the Economic Geology Research Centre (EGRU) at James Cook University (Townsville), and Exploration Data Centre in Brisbane, for supporting us in conducting this research.

**Author contribution** Fieldwork was conducted by AAK and IS; analyses by AAK and HEC; manuscript conceptualization and illustration was written jointly by AAK, IS, and HEC; text edited and modified by PHGMD. All authors read and approved the final manuscript.

**Funding** Open Access funding enabled and organized by CAUL and its Member Institutions

**Data availability** Supplementary material provided.

## Declarations

**Conflict of interest** The authors declare no competing interests.

**Open Access** This article is licensed under a Creative Commons Attribution 4.0 International License, which permits use, sharing, adaptation, distribution and reproduction in any medium or format, as long as you give appropriate credit to the original author(s) and the source, provide a link to the Creative Commons licence, and indicate if changes were made. The images or other third party material in this article are included in the article's Creative Commons licence, unless indicated otherwise in a credit line to the material. If material is not included in the article's Creative Commons licence and your intended use is not permitted by statutory regulation or exceeds the permitted use, you will need to obtain permission directly from the copyright holder. To view a copy of this licence, visit <http://creativecommons.org/licenses/by/4.0/>.

## References

- Andersen JC , Stickland RJ, Rollinson GK, Shail RK (2016) Indium mineralisation in SW England: host parageneses and mineralogical relations. *Ore Geol Rev* 78:213–238. <https://doi.org/10.1016/j.oregeorev.2016.02.019>
- Bailey JC, Morgan WR, Black LP (1982) Geochemical and isotopic evidence for the age, orogenic setting and petrogenesis of the Nychum Volcanic association, North Queensland. *J Geol Soc Aust* 29:375–393. <https://doi.org/10.1080/00167618208729221>
- Bauer ME, Burisch M, Ostendorf J et al (2019a) Trace element geochemistry of sphalerite in contrasting hydrothermal fluid systems of the Freiberg district, Germany: insights from LA-ICP-MS analysis, near-infrared light microthermometry of sphalerite-hosted fluid inclusions, and sulfur isotope geochemistry. *Miner Depos* 54:237–262. <https://doi.org/10.1007/s00126-018-0850-0>
- Bauer ME, Seifert T, Burisch M et al (2019b) Indium-bearing sulfides from the H ammerlein skarn deposit, Erzgebirge, Germany: evidence for late-stage diffusion of indium into sphalerite. *Miner Depos* 54:175–192. <https://doi.org/10.1007/s00126-017-0773-1>
- Bethke CM, Farrell B, Yeakel S (2022) The Geochemist's Workbench, Version 12.0: GWB Essentials Guide. Illinois, US LLC Champaign
- Blanc Ph, Lassin A, Piantone P et al (2012) Thermodden: a geochemical database focused on low temperature water/rock interactions and waste materials. *Appl Geochem* 27:2107–2116. <https://doi.org/10.1016/j.apgeochem.2012.06.002>
- Boschetti T (2023) An update on lithium mica thermodynamics and its geothermometrical application. *Geothermics* 109:102661. <https://doi.org/10.1016/j.geothermics.2023.102661>
- Brill BA (1989) Trace-element contents and partitioning of elements in ore minerals from the CSA Cu-Pb-Zn Deposit, Australia, and implications for ore genesis. *Can Mineral* 27:263–274
- Carvalho JRS, Relvas JMRS, Pinto AMM et al (2018) Indium and selenium distribution in the Neves-Corvo deposit, Iberian Pyrite Belt, Portugal. *Mineral Mag* 82:S5–S41. <https://doi.org/10.1180/minmag.2017.081.079>
- Champion DC (1991) The felsic granites of far north Queensland (PhD thesis). The Australian National University, Canberra, Australia
- Champion DC, Bultitude RJ (2013) The geochemical and Sr-Nd isotopic characteristics of Paleozoic fractionated S-types granites of north Queensland: implications for S-type granite petrogenesis. *Lithos* 162–163:37–56. <https://doi.org/10.1016/j.lithos.2012.11.022>
- Cheng Y, Spandler C, Chang Z, Clarke G (2018) Volcanic–plutonic connections and metal fertility of highly evolved magma systems: a case study from the Herberton Sn–W–Mo Mineral Field, Queensland, Australia. *Earth Planet Sci Lett* 486:84–93. <https://doi.org/10.1016/j.epsl.2018.01.012>
- Cook NJ, Ciobanu CL, Pring A et al (2009) Trace and minor elements in sphalerite: a LA-ICPMS study. *Geochim Cosmochim Acta* 73:4761–4791. <https://doi.org/10.1016/j.gca.2009.05.045>
- Cook NJ, Ciobanu CL, Brugger J et al (2012) Determination of the oxidation state of Cu in substituted Cu-In-Fe-bearing sphalerite via -XANES spectroscopy. *Am Miner* 97:476–479. <https://doi.org/10.2138/am.2012.4042>
- Dill HG, Garrido MM, Melcher F et al (2013) Sulfidic and non-sulfidic indium mineralization of the epithermal Au–Cu–Zn–Pb–Ag deposit San Roque (Provincia Rio Negro, SE Argentina) — with special reference to the “indium window” in zinc sulfide. *Ore Geol Rev* 51:103–128. <https://doi.org/10.1016/j.oregeorev.2012.12.005>
- Donovan JJ, Snyder DA, Rivers ML (1992) An improved interference correction for trace element analysis. In: Proceedings of the Annual Meeting-Electron Microscopy Society of America. San Francisco Press 1646
- Drouin D, Couture AR, Joly D et al (2007) CASINO V2.42—a fast and easy-to-use modeling tool for scanning electron microscopy and microanalysis users. *Scanning* 29:92–101. <https://doi.org/10.1002/sca.20000>
- Edgar A, Sanislav IV, Dirks PHGM, Spandler C (2022b) Metamorphic diamond from the northeastern margin of Gondwana: paradigm shifting implications for one of Earth's largest orogens. *Sci Adv* 8:2811. <https://doi.org/10.1126/sciadv.abo2811>

- Edgar A, Sanislav IV, Dirks PHGM (2022a) Tectonic setting and mineralisation potential of the Cowley Ophiolite Complex, north Queensland. *Australian Journal of Earth Sciences* 1–17. <https://doi.org/10.1080/08120099.2022.2086173>
- Fontana D, Forte F, Pietrantonio M, Pucciarmati S (2021) Recent developments on recycling end-of-life flat panel displays: a comprehensive review focused on indium. *Crit Rev Environ Sci Technol* 51:429–456. <https://doi.org/10.1080/10643389.2020.1729073>
- Frenzel M, Mikolajczak C, Reuter MA, Gutzmer J (2017) Quantifying the relative availability of high-tech by-product metals – the cases of gallium, germanium and indium. *Resour Policy* 52:327–335. <https://doi.org/10.1016/j.resourpol.2017.04.008>
- George LL, Cook NJ, Crowe BBP, Ciobanu CLL (2018) Trace elements in hydrothermal chalcocopyrite. *Mineral Mag* 82:59–88. <https://doi.org/10.1180/minmag.2017.081.021>
- Henderson RA, Donchak PJT, Withnall IW (2013) Mossman Orogen. In: Jell PA (ed) *Geology of Queensland*. Geological Survey of Queensland 225–304
- Henderson RA, Fergusson CL (2019) Growth and provenance of a Paleozoic subduction complex in the Broken River Province, Mossman Orogen: evidence from detrital zircon ages. *Aust J Earth Sci* 66:607–624. <https://doi.org/10.1080/08120099.2019.1572033>
- Henke BL, Gullikson EM, Davis JC (1993) X-ray interactions: photoabsorption, scattering, transmission, and reflection at  $E = 50\text{--}30,000$  eV,  $Z = 1\text{--}92$ . *At Data Nucl Data Tables* 54:181–342. <https://doi.org/10.1006/adnd.1993.1013>
- Hutchison MN, Scott SD (1981) Sphalerite geobarometry in the Cu-Fe-Zn-S system. *Econ Geol* 76:143–153. <https://doi.org/10.2113/gsecongeo.76.1.143>
- Ishihara S, Murakami H, Marquez-Zavalía MF (2011) Inferred indium resources of the Bolivian tin-polymetallic deposits. *Resour Geol* 61:174–191. <https://doi.org/10.1111/j.1751-3928.2011.00157.x>
- Johan Z (1988) Indium and germanium in the structure of sphalerite: an example of coupled substitution with Copper. *Mineral Petrol* 39:211–229. <https://doi.org/10.1007/BF01163036>
- Kojima S, Sugaki A (1985) Phase relations in the Cu-Fe-Zn-S system between 500 degrees and 300 degrees C under hydrothermal conditions. *Econ Geol* 80:158–171. <https://doi.org/10.2113/gsecongeo.80.1.158>
- Korges M, Weis P, Lüders V, Laurent O (2020) Sequential evolution of Sn–Zn–In mineralization at the skarn-hosted Hämmerlein deposit, Erzgebirge, Germany, from fluid inclusions in ore and gangue minerals. *Miner Depos* 55:937–952. <https://doi.org/10.1007/s00126-019-00905-4>
- Kumar AA, Sanislav IV, Dirks PHGM (2022) The geological setting of the indium-rich Baal Gammon and Isabel Sn-Cu-Zn deposits in the Herberton Mineral Field, Queensland, Australia. *Ore Geol Rev* 149:105095. <https://doi.org/10.1016/j.oregeorev.2022.105095>
- Lehmann B (2021) Formation of tin ore deposits: a reassessment. *Lithos* 402–403:105756. <https://doi.org/10.1016/j.lithos.2020.105756>
- Li B, Li N-X, Yang J-N et al (2023) Genesis of the Xianghualing tin-polymetallic deposit in southern Hunan, South China: constraints from chemical and boron isotopic compositions of tourmaline. *Ore Geol Rev* 154:105303. <https://doi.org/10.1016/j.oregeorev.2023.105303>
- Liu J, Rong Y, Zhang S et al (2017) Indium mineralization in the Xianghualing Sn-polymetallic orefield in southern Hunan, Southern China. *Minerals* 7:1–26. <https://doi.org/10.3390/min7090173>
- Llovet X, Moy A, Pinard PT, Fournelle JH (2021) Electron probe microanalysis: a review of recent developments and applications in materials science and engineering. *Prog Mater Sci* 116:100673. <https://doi.org/10.1016/j.pmatsci.2020.100673>
- Murakami H, Ishihara S (2013) Trace elements of Indium-bearing sphalerite from tin-polymetallic deposits in Bolivia, China and Japan: a femto-second LA-ICPMS study. *Ore Geol Rev* 53:223–243. <https://doi.org/10.1016/j.oregeorev.2013.01.010>
- Nekrasov IJ, Sorokin VI, Osadchii EG (1979) Fe and Zn partitioning between stannite and sphalerite and its application in geothermometry. *Phys Chem Earth* 11:739–742. [https://doi.org/10.1016/0079-1946\(79\)90069-7](https://doi.org/10.1016/0079-1946(79)90069-7)
- Poblete JA, Dirks PHGM, Chang Z et al (2021) The Watershed Tungsten Deposit, Northeast Queensland, Australia: Permian Metamorphic Tungsten Mineralization Overprinting Carboniferous Magmatic Tungsten. *Econ Geol* 116:427–451. <https://doi.org/10.5382/econgeo.4791>
- Pouchou J-L, Pichoir F (1991) Quantitative analysis of homogeneous or stratified microvolumes applying the model “PAP.” *Electron Probe Quantitation*. Springer, US, Boston, MA, pp 31–75
- Schorr S, Wagner G (2005) Structure and phase relations of the  $\text{Zn}_{2x}(\text{CuIn})_{1-x}\text{S}_2$  solid solution series. *J Alloys Compd* 396:202–207. <https://doi.org/10.1016/j.jallcom.2004.12.018>
- Schorr S, Riede V, Spemann D, Doering Th (2006) Electronic band gap of  $\text{Zn}_{2x}(\text{CuIn})_{1-x}\text{X}_2$  solid solution series ( $\text{X}=\text{S}, \text{Se}, \text{Te}$ ). *J Alloys Compd* 414:26–30. <https://doi.org/10.1016/j.jallcom.2005.07.014>
- Schuffe JA, Stubbs MF, Witman RE (1951) A study of indium(III) chloride complexes by polarographic methods. *J Am Chem Soc* 73:1013–1015. <https://doi.org/10.1021/ja01147a038>
- Schwarz-Schampera U, Herzig PM (2002) Indium: geology, mineralogy, and economics. Springer Science & Business Media
- Seifert T, Sandmann D (2006) Mineralogy and geochemistry of indium-bearing polymetallic vein-type deposits: implications for host minerals from the Freiberg district Eastern Erzgebirge, Germany. *Ore Geol Rev* 28:1–31. <https://doi.org/10.1016/j.oregeorev.2005.04.005>
- Seward TM, Henderson CMB, Charnock JM (2000) Indium(III) chloride complexing and solvation in hydrothermal solutions to 350°C: an EXAFS study. *Chem Geol* 167:117–127. [https://doi.org/10.1016/S0009-2541\(99\)00204-1](https://doi.org/10.1016/S0009-2541(99)00204-1)
- Seward TM, Williams-Jones AE, Migdisov AA (2014) The chemistry of metal transport and deposition by ore-forming hydrothermal fluids. In: *Treatise on Geochemistry*, 2nd edn. Elsevier 29–57
- Shimizu M, Shikazono N (1985) Iron and zinc partitioning between coexisting stannite and sphalerite: a possible indicator of temperature and sulfur fugacity. *Miner Depos* 20:314–320. <https://doi.org/10.1007/BF00204292>
- Simmons SF, Brown KL, Tutolo BM (2016) Hydrothermal transport of Ag, Au, Cu, Pb, Te, Zn, and other metals and metalloids in New Zealand geothermal systems: spatial patterns, fluid-mineral equilibria, and implications for epithermal mineralization. *Econ Geol* 111:589–618. <https://doi.org/10.2113/econgeo.111.3.589>
- Sinclair WD, Kooiman GJA, Martin DA, Kjarsgaard IM (2006) Geology, geochemistry and mineralogy of indium resources at Mount Pleasant, New Brunswick, Canada. *Ore Geol Rev* 28:123–145. <https://doi.org/10.1016/j.oregeorev.2003.03.001>
- Sugaki A, Shima H, Kitakaze A, Harada H (1975) Isothermal phase relations in the system Cu-Fe-S under hydrothermal conditions at 350 degrees C and 300 degrees C. *Econ Geol* 70:806–823. <https://doi.org/10.2113/gsecongeo.70.4.806>
- Sugaki A, Kitakaze A, Ueno T (1982) Hydrothermal synthesis of minerals in the system Cu-Fe-S and their phase equilibrium at 400° C and 500° C. *J Japan Assoc Mineral Petrol Econ Geol* 77:257–269
- Torres, Melgarejo, Torró et al (2019) The Poopó polymetallic epithermal deposit, Bolivia: mineralogy, genetic constraints, and distribution of critical elements. *Minerals* 9:472. <https://doi.org/10.3390/min9080472>
- Torró, Cazorla, Melgarejo et al (2019a) Indium mineralization in the volcanic dome-hosted Animas–Chocaya–Siete Suyos Polymetallic Deposit, Potosí. *Bolivia Miner* 9:604. <https://doi.org/10.3390/min9100604>
- Torró L, Melgarejo J, Gemmrich L et al (2019b) Spatial and temporal controls on the distribution of indium in Xenothermal Vein-deposits: the Huari Huari District, Potosí. *Bolivia Miner* 9:304. <https://doi.org/10.3390/min9050304>

- Valkama M, Sundblad K, Nygård R, Cook N (2016) Mineralogy and geochemistry of indium-bearing polymetallic veins in the Sarvlaxviken area, Lovisa, Finland. *Ore Geol Rev* 75:206–219. <https://doi.org/10.1016/j.oregeorev.2015.12.001>
- Voudouris P, Repstock A, Spry PG et al (2022) Physicochemical constraints on indium-, tin-, germanium-, gallium-, gold-, and tellurium-bearing mineralizations in the Pefka and St Philippos polymetallic vein- and breccia-type deposits, Greece. *Ore Geol Rev* 140:104348. <https://doi.org/10.1016/j.oregeorev.2021.104348>
- Watari T, Nansai K, Nakajima K (2020) Review of critical metal dynamics to 2050 for 48 elements. *Resour Conserv Recycl* 155:104669. <https://doi.org/10.1016/j.resconrec.2019.104669>
- Werner TT, Mudd GM, Jowitt SM (2017) The world's by-product and critical metal resources part III: a global assessment of indium. *Ore Geol Rev* 86:939–956. <https://doi.org/10.1016/j.oregeorev.2017.01.015>
- White AJR, Allen CM, Beams SD et al (2001) Granite suites and super-suites of eastern Australia. *Aust J Earth Sci* 48:515–530. <https://doi.org/10.1046/j.1440-0952.2001.00874.x>
- Wiggins LB, Craig JR (1980) Reconnaissance of the Cu-Fe-Zn-S system; sphalerite phase relationships. *Econ Geol* 75:742–751. <https://doi.org/10.2113/gsecongeo.75.5.742>
- Wood SA, Samson IM (2006) The aqueous geochemistry of gallium, germanium, indium and scandium. *Ore Geol Rev* 28:57–102. <https://doi.org/10.1016/j.oregeorev.2003.06.002>
- Xu J, Ciobanu CLL, Cook NJ et al (2021) Phase relationships in the system ZnS-CuInS<sub>2</sub>: Insights from a nanoscale study of indium-bearing sphalerite. *Am Mineral* 106:192–205. <https://doi.org/10.2138/am-2020-7488>

**Publisher's note** Springer Nature remains neutral with regard to jurisdictional claims in published maps and institutional affiliations.